III-V Nanostructures for

Photovoltaic Applications

Dongyoung Kim

A thesis submitted to University College London for the degree of

Doctor of Philosophy (PhD)

Department of Electronic & Electrical Engineering

University College London

November 2018

Statement of Originality

I, Dongyoung Kim, confirm that the work presented in this thesis is my own. Where information has been derived from other sources, I confirm that this has been indicated in the thesis.

Signed:

Date:

To my grandmother, Ms Youngja Lee (이영자),
and my grandfather Mr Sangtae Kim (김상태).
이 모든것을 가능하게 해주신 할머니 할아버지께 이 논문을 바칩니다.

Abstract

The concept of introducing an intermediate band to overcome the efficiency limit of single-bandgap solar cells was proposed by Luque and Martí in 1997. It is predicted that utilising the intermediate band for multi-photon absorption can significantly improve the photocurrent generation without accompanying output voltage loss. Amongst several approaches to develop an intermediate band solar cell, quantum dots have drawn much attention as intermediate band due to their three-dimensional quantum confinement and bandgap tunability. However, despite the effort expended so far, there still remains several major challenges that prevent the successful implementation of quantum dot intermediate band solar cells.

The work reported in this thesis aims to provide solutions to the main challenges in implementing high-efficiency quantum dot solar cells. The work involves the design, epitaxial growth by molecular beam epitaxy, device processing, and characterisation of QDSCs. This thesis first investigates the influence of direct Si doping on InAs/GaAs quantum dot solar cells with AlAs cap layers. Si doping in QDs leads to state filling of the intermediate band, which is one of the key requirements for a high-efficiency intermediate band solar cell. Moreover, the introduction of moderate amount of Si dopants leads to passivation of defect states, and

hence prolongs the carrier lifetime and increases the open-circuit voltage. Secondly, type-II InAs/GaAsSb quantum dot solar cells are studied. Increased photocurrent contribution from the quantum dot region is observed due to the prolonged carrier lifetime associated with the type-II band alignment. Lastly, different types and positions of quantum dot doping methods are investigated. The photoluminescence spectra indicate that using delta or modulation doping in quantum dots can reduce the degradation of crystal quality, and hence decrease the number of non-radiative recombination centres, when compared with using direct doping.

Impact Statement

In recent years, there has been increasing interest in renewable energy due to the growing environmental concerns associated with fossil fuel exploitation, and the uncertainty about the future direction of oil prices. Solar energy is often said to be the most appealing of all renewable energy sources as the it is abundantly and readily available globally. Since the invention of the first crystalline Si-based solar cell by Bell Labs in 1954, single-crystal Si solar cells have matured and reached an efficiency of ~25 %. However, using Si for solar energy conversion is not ideal as Si is an indirect bandgap semiconductor material. Furthermore, the maximum theoretical efficiency of single-junction solar cells is limited by the inability to absorb sub-bandgap photons, and by the thermalisation of electron-hole pairs produced by supra-bandgap photons. This makes the optical absorption in single-crystal Si solar cells inefficient, and limits the maximum efficiency under one-sun illumination to ~29 %.

For space and military applications, where high-efficiency, low-volume, and lightweight solar cells are needed, a range of III-V semiconductor materials has been studied. In particular, self-assembled III-V quantum dots have been intensely investigated since the concept of the intermediate band solar cell was proposed by Luque and Martí in 1997. Due to their

three-dimensional quantum confinement and bandgap tunability, quantum dots have been proposed as means of implementing an intermediate band in a solar cell. Use of quantum dots could overcome the Shockley-Queisser efficiency limit by harvesting a larger portion of the solar spectrum with respect to the host bulk semiconductor. The findings presented in this thesis provide solutions to main challenges in implementing high-efficiency III-V quantum dot solar cells, and bring us a step closer to realising the high efficiencies for quantum dot collar cells predicted by the intermediate band theoretical model.

Acknowledgements

First and foremost, I would like to thank my supervisor, Prof. Huiyun Liu, who has been an inspiration to me since my undergraduate years, for his guidance, patience, and support during my PhD study. Without his supervision, none of the work presented in this thesis would have been possible. I would also like to show my gratitude to my second supervisor, Dr Jiang Wu, for helping me develop an understanding of the physics of solar cells.

I would like to acknowledge all current and former members of the Molecular Beam Epitaxy Research Group and its football team, Gower United FC: Dr Siming Chen, Dr Yunyan Zhang, Dr Mingchu Tang, Dr Pamela Jurczak, Mr Kevin Lee, Dr Arthur Onno, Dr Sabina Hatch, Dr Qi Jiang, Dr Phu-Minh Lam, Dr. João Valente, Dr Xuezhe Yu, Dr Jae-Seong Park, Mr Hao Xu, Ms Mengya Liao, Mr Daqian Guo, and Mr Shun Chan. The research group has been a source of friendship as well as good advice and collaboration.

Table of Contents

Table of Figures

Table of Tables

List of Publications

Journal Publications:

1. **<u>D. Kim,</u>** S. Hatch, J. Wu, K. A. Sablon, P. Lam, P. Jurczak, M. Tang, W. P. Gillin, and H. Liu, 'Type-II InAs/GaAsSb Quantum Dot Solar Cells With GaAs Interlayer', *IEEE Journal of Photovoltaics*, vol. 8, no. 3, pp. 741–745, May. 2018.

2. **<u>D. Kim</u>**, M. Tang, J. Wu, S. Hatch, Y. Maidaniuk, V. Dorogan, Y.I. Mazur, G.J. Salamo, H. Liu, 'Si-Doped InAs/GaAs Quantum-Dot Solar Cell With AlAs Cap Layers', *IEEE Journal of Photovoltaics*, vol. 6, no. 4, pp. 906–911, Jul. 2016.

3. F. Cappelluti, **<u>D. Kim</u>**, M. van Eerden, A. P. Cédola, T. Aho, G. Bissels, F. Elsehrawy, J. Wu, H. Liu, P. Mulder, G. Bauhuis, J. Schermer, T. Niemi, and M. Guina, "Light-trapping enhanced thin-film III-V quantum dot solar cells fabricated by epitaxial lift-off," *Solar Energy Materials and Solar Cells*, Jan. 2018.

4. A. P. Cédola, **<u>D. Kim</u>**, A. Tibaldi, M. Tang, A. Khalili, J. Wu, H. Liu, and F. Cappelluti, "Physics-Based Modeling and Experimental Study of Si-Doped InAs/GaAs Quantum Dot Solar Cells," *International Journal of Photoenergy*, 2018.

5. H. Xu, X. Han, X. Dai, W. Liu, J. Wu, J. Zhu, **D. Kim**, G. Zou, K. A. Sablon, A. Sergeev, Z. Guo, and H. Liu, "High Detectivity and Transparent Few-Layer MoS2/Glassy-Graphene Heterostructure Photodetectors," *Advanced Materials*, vol. 30, no. 13, p. 1706561, Jan. 2018.

6. Y. Zhang, Z. Sun, A. M. Sanchez, M. Ramsteiner, M. Aagesen, J. Wu, **D. Kim**, P. Jurczak, S. Huo, L. J. Lauhon, and H. Liu, "Doping of Self-Catalyzed Nanowires under the Influence of Droplets," *Nano Lett.*, vol. 18, no. 1, pp. 81–87, Jan. 2018.

7. Y. Zhang, H. A. Fonseka, M. Aagesen, J. A. Gott, A. M. Sanchez, J. Wu, **D. Kim**, P. Jurczak, S. Huo, and H. Liu, "Growth of Pure Zinc-Blende GaAs(P) Core–Shell Nanowires with Highly Regular Morphology," *Nano Lett.*, vol. 17, no. 8, pp. 4946–4950, Aug. 2017.

8. P. Lam, J. Wu, M. Tang, **D. Kim**, S. Hatch, I. Ramiro, V.G. Dorogan, M. Benamara, Y.I. Mazur, G.J. Salamo, J. Wilson, R. Allison, H. Liu, 'InAs/InGaP quantum dot solar cells with an AlGaAs interlayer', S*olar Energy Materials and Solar Cells*, vol. 144, pp. 96–101, Jan. 2016.

9. J. Wu, A. Ramsay, A. Sanchez, Y. Zhang, **D. Kim**, F. Brossard, X. Hu, M. Benamara, M.E. Ware, Y.I. Mazur, G.J. Salamo, M. Aagesen, Z. Wang, H. Liu, 'Defect-Free Self-Catalyzed GaAs/GaAsP Nanowire Quantum Dots Grown on Silicon Substrate', *Nano Letters*, vol. 16, no. 1, pp. 504–511, Jan. 2016.

10. Y. Zhang, A.M. Sanchez, Y. Sun, J. Wu, M. Aagesen, S. Huo, **D. Kim**, P. Jurczak, X. Xu, H. Liu, 'Influence of Droplet Size on the Growth of Self-Catalyzed Ternary GaAsP Nanowires', *Nano Letters*, vol. 16, no. 2, pp. 1237–1243, Feb. 2016.

11. P. Lam, J. Wu, S. Hatch, **D. Kim**, M. Tang, H. Liu, J. Wilson, R. Allison, 'The Effect of Rapid Thermal Annealing on InAs/GaAs Quantum Dot Solar Cells', *IET Optoelectronics*, 2014.

Conference Presentations:

1. **D. Kim**, J. Wu, A. Govorov, Z. Wang, 'Plasmon-enhanced quantum dot solar cells', META 2018: the 9th International Conference on Metamaterials, Photonic Crystals and Plasmonics, Marseille, France, 2018. *(Invited talk)*

2. **D. Kim**, S. Chan, M. Tang, J. Wu, H Liu, 'The influence of direct, delta, and modulation QD Si doping', WCPEC-7: the 45th IEEE PVSC, the 28th PVSEC, Waikoloa, HI, United States, 2018.

3. **D. Kim**, M. Tang, J. Wu, S. Hatch, Y. Maidaniuk, V. Dorogan, Y.I. Mazur, G.J. Salamo, H. Liu, 'The influence of Si doping on InAs/GaAs quantum dot solar cells with AlAs cap layers', *SPIE Photonics West,* San Francisco, CA, United States, 2017.

4. **D. Kim**, M. Tang, J. Wu, S. Hatch, Y. Maidaniuk, V. Dorogan, Y.I. Mazur, G.J. Salamo, H. Liu, 'The influence of Si doping on InAs/GaAs quantum dot solar cells with AlAs cap layers', *European Space Power Conference,* Thessaloniki, Greece, 2016.

5. **D. Kim**, M. Tang, J. Wu, S. Hatch, Y. Maidaniuk, V. Dorogan, Y.I. Mazur, G.J. Salamo, H. Liu, 'Si-doped InAs/GaAs quantum dot solar cell with AlAs cap layers', *International Conference on MBE,* Montpellier, France, 2016.

6. **D. Kim**, M. Tang, J. Wu, S. Hatch, Y. Maidaniuk, V. Dorogan, Y.I. Mazur, G.J. Salamo, H. Liu, 'Si-doped InAs/GaAs quantum dot solar cell with AlAs cap layers', *UK Semiconductors,* Sheffield, UK, 2016.

7. **D. Kim**, M. Tang, J. Wu, S. Hatch, Y. Maidaniuk, V. Dorogan, Y.I. Mazur, G.J. Salamo, H. Liu, 'State filling effects in Si-doped InAs/GaAs quantum dot solar cell with AlAs cap layers', *Semiconductor and Integrated Optoelectronics,* Cardiff, UK, 2016.

8. **D. Kim**, J. Wu, M. Tang, S. Hatch, I. Ramiro, V. G. Dorogan, M. Benamara, Y. I. Mazur, G. J. Salamo, J. Wilson, R. Allison, H. Liu, 'InAs/InGaP quantum dot solar cells with an AlGaAs interlayer', *UK Semiconductors,* Sheffield, UK, 2015.

9. **<u>D. Kim</u>**, S. Hatch, J. Wu, H. Liu, 'Type-II hybrid InAs QD/GaAsSb QW solar cells with GaAs interlayer', *Semiconductor and Integrated Optoelectronics,* Cardiff, UK, 2015.

Chapter 1
Introduction to solar energy and solar cells

It is essential to understand the interaction between light and semiconductors in order to understand solar cells. This chapter aims to, firstly, explore the nature of the solar resource and semiconductor materials used for photovoltaic applications, and secondly, introduce and discuss the concepts of the multi-junction solar cell, intermediate band quantum dot solar cell, and nanowire solar cell.

1.1 The solar resource

Due to the uncertain availability, severe environmental impacts, and the increasing cost of conventional energy sources, such as fossil fuels, the interest in solar energy is on the increase. In order to utilise solar resources, the insolation needs to be converted to a different form. There are several forms of solar energy conversion, namely, solar thermal (sunlight to heat), solar thermal-electric (sunlight to heat, and then to electricity), biomass

(sunlight to biomass, and then to fuels), and photovoltaics (sunlight to electricity) [1].

The earth receives energy from the sun via radiation, of which the balance determines the climate of the planet and drives the planet's weather and ecosystem. The wavelength of sunlight ranges from the ultraviolet to the infrared part of the electromagnetic spectrum with the highest irradiance at the visible wavelength (300 – 800 nm). The amount of solar radiation energy received on the surface of the Earth changes throughout the year due to the elliptical orbit of the Earth around the sun and the fluctuating power emitted by the Sun. It also depend on the time of the day, atmospheric conditions, and location (e.g. the amount of the solar energy received in the UK in a year is about 60 % of that on the equator [2]). In order to allow the comparison between different solar cells from various manufacturers and laboratories, standard solar spectra have been set by the photovoltaic research community and the American Society for Testing and Materials (ASTM). The standard spectra are based on air mass that indicates the relative path length to the zenith at sea level. As shown in Figure 1.1, air mass (AM) is zero at the region above the atmosphere, otherwise is defined as Equation 1.1.

$$AM = \sec \theta_z$$

(θ_z: zenith angle)

Equation 1.1

Zenit

AM 1.5
$\theta_z = 48.2\,°$

(θ_z: zenith angle)

AM 2.0
$\theta_z = 60.1\,°$
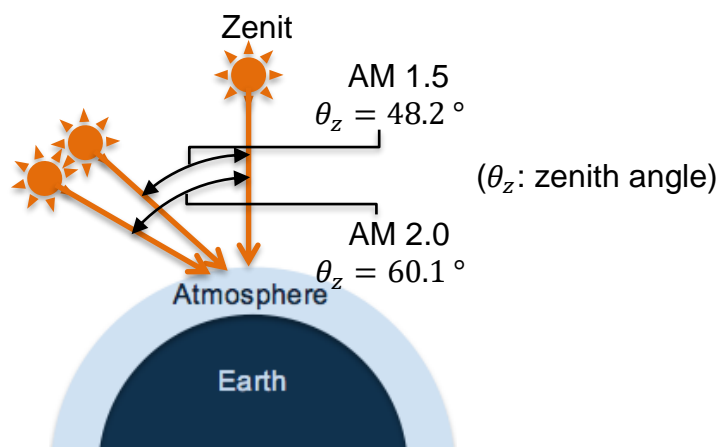
Atmosphere

Earth

Figure 1.1 Schematic diagram of air mass.

The surface of the sun emits a power density of 6.2 × 10^7 W m^{-2}. The solar flux is lower at a point just outside the atmosphere of the Earth due to the reduced angular range of the sun, which gives 1,353 W m^{-2} [3]. This extra-terrestrial spectrum, which is the standard used for space solar cell applications, is referred to as AM0. The Earth's surface receives only 70 % of the AM0 due to atmospheric scattering and absorption. For terrestrial applications, AM1.5 Global and AM1.5 Direct are used for flat panel

modules and solar concentrator applications, respectively. As shown in Figure 1.1, AM1.5 is given at a zenith angle of 48 °, and is defined as the total spectrum incident on a horizontal plane taking the diffused components and albedo effects into account. The power density of the AM1.5 Global spectrum is measured to be around 900 Wm-2, however, the standard value for the power density of AM1.5 Global at 25 °C was set at 1000 Wm-2 for convenience [4]. On the other hand, AM1.5 Direct consists of only the direct normal component that contributes to the total global spectrum, with standard integrated power density of 900 Wm-2. The standard solar spectra of AM0, AM1.5 Global, and AM1.5 Direct are shown in Figure 1.2.
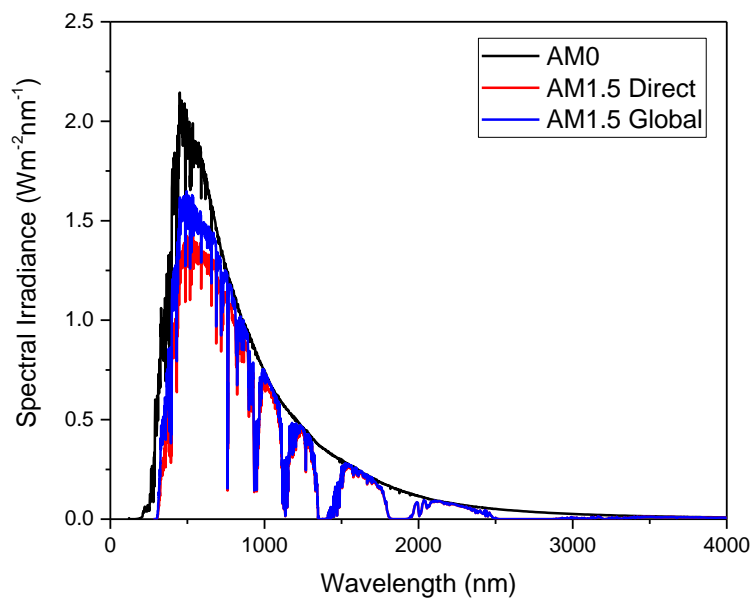
Figure 1.2 The extra-terrestrial spectrum, AM0, and the terrestrial spectra, AM1.5 Global and AM1.5 Direct [4].

1.2   Semiconductor materials

In semiconductor materials, electrons can be transferred from the valence band (VB) to the conduction band (CB) by absorbing photons that have higher energy than the bandgap of the materials. The absorbed energy can cause the breaking of the covalent bonds and the creation of electron-hole pairs, which is the fundamental principle of photovoltaic energy production. In this process, the excess energy above the bandgap is dissipated as head in the lattice structure. On the other hand, photons with the lower energy than the bandgap of the material, sub-bandgap photons, pass through the semiconductor without being absorbed. The electron-hole pairs created by photon absorption can recombine if they stay within the semiconductor material for long enough. This recombination process can be assisted by defects and impurities in the semiconductor material. High-energy photons have shorter absorption depths and are absorbed near the front surface of the semiconductor. On the other hand, low-energy photons are absorbed further away from the front surface as they have greater absorption depths. The generation rate is defined as the number of created electron-hole pairs per unit volume, as shown in Equation 1.2.

$$G(x) = \alpha N e^{-\alpha x}$$

(G: generation rate

x: distance from the front surface into the semiconductor material

α: absorption coefficient

N: photon flux)

Equation 1.2

The absorption coefficient, α, is a measure of the distance from the front surface, x , that photons with particular energy are absorbed in a semiconductor material. Figure 1.3 [5] shows the shows the absorption coefficient, α, as a function of wavelength and photon energy for various semiconductors. It can be seen that in indirect bandgap semiconductors, such as Si, there is a long tail in absorption towards lower energy region.
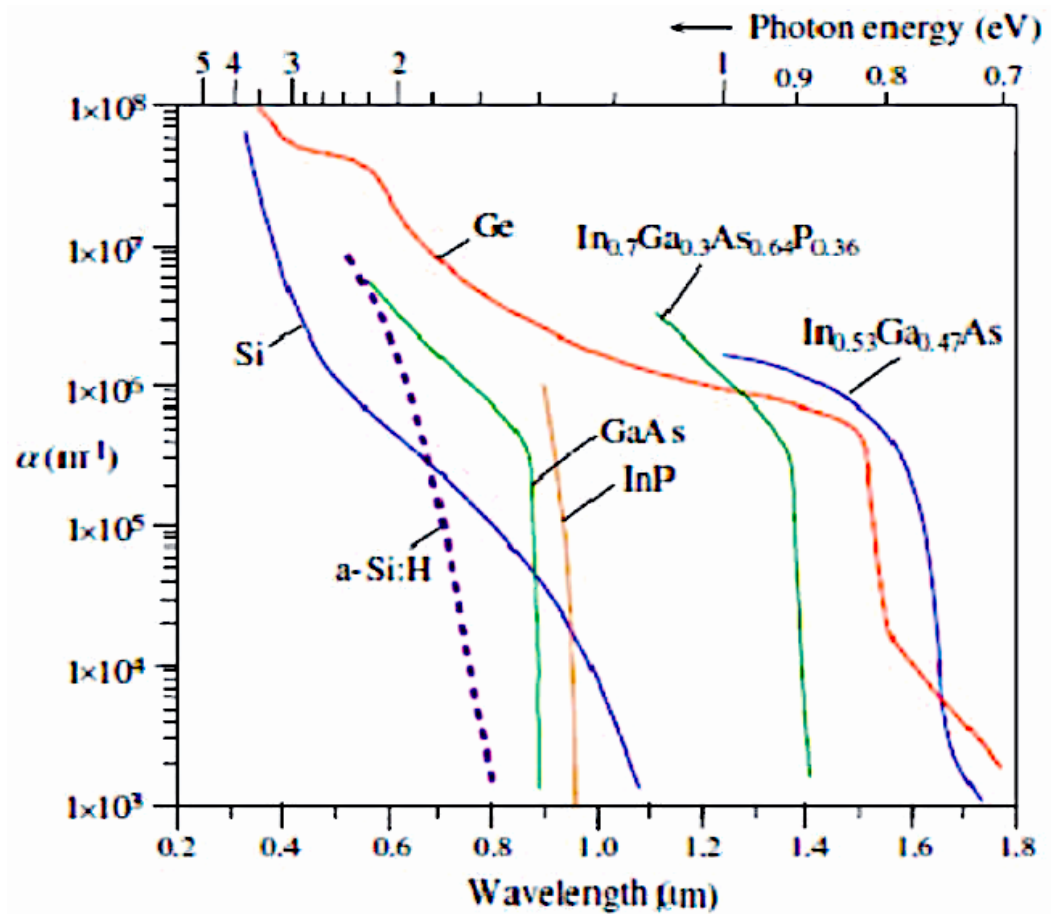
Figure 1.3 Absorption coefficient, α, as a function of wavelength for various semiconductors [5].

The most commonly used semiconductor material for photovoltaic applications is Si, however, depending on the optical characteristics, cost, and yield required by applications, II-VI compounds, such as CdTe, and III-V compounds, such as GaAs, are also used.

1.3   P-N junction

Most semiconductor optoelectronic devices are based on p-n junctions formed by joining p-type and n-type semiconductor materials. Their optical and electronic processes depend on the properties of the p-n junction. Electrons diffuse from the n-type side of the p-n junction to the p-type side due to the high concentration of electrons of the former and the high holes concentration of the latter. In the same manner, holes are diffused from the p-type side to the n-type side. At the boundary, a depletion region is formed by the diffusion of electrons from the n-type into the p-type and holes from the p-type into the n-type. Further diffusion across the junction is prevented by the electric field formed at the boundary.

When voltage is applied to the junction, the electric field can be either decreased to promote the diffusion (forward bias), or increased to suppress the diffusion (reverse bias). The flow of current through a p-n junction is described by the diode equation derived by Shockley [6], as shown in Equation 1.3.

$$I = I_0 \left(e^{\frac{qV}{nkT}} - 1 \right)$$

(I: net current flowing through the diode

I_0: dark saturation current

V: applied voltage across the terminals of the diode

q: absolute value of electron charge

n: ideality factor

k: Boltzmann's constant

T: absolute temperature (K))

Equation 1.3

In this equation, it is assumed that the junction is abrupt and there is no generation or recombination in the depletion region. The Shockley current, I, in Equation 1.3 is also referred to as dark current, I_D, in relation to solar cells. The dark saturation current, I_0, is the leakage current in the absence of light, and n is the ideality factor. In an ideal diode, where all recombination is radiative and occurs in the bulk of the device, the ideality factor is equal to 1. However, in practice, other parts of the device are involved in recombination and the recombination could be non-radiative, in which case the ideality factor is between 1 and 2.
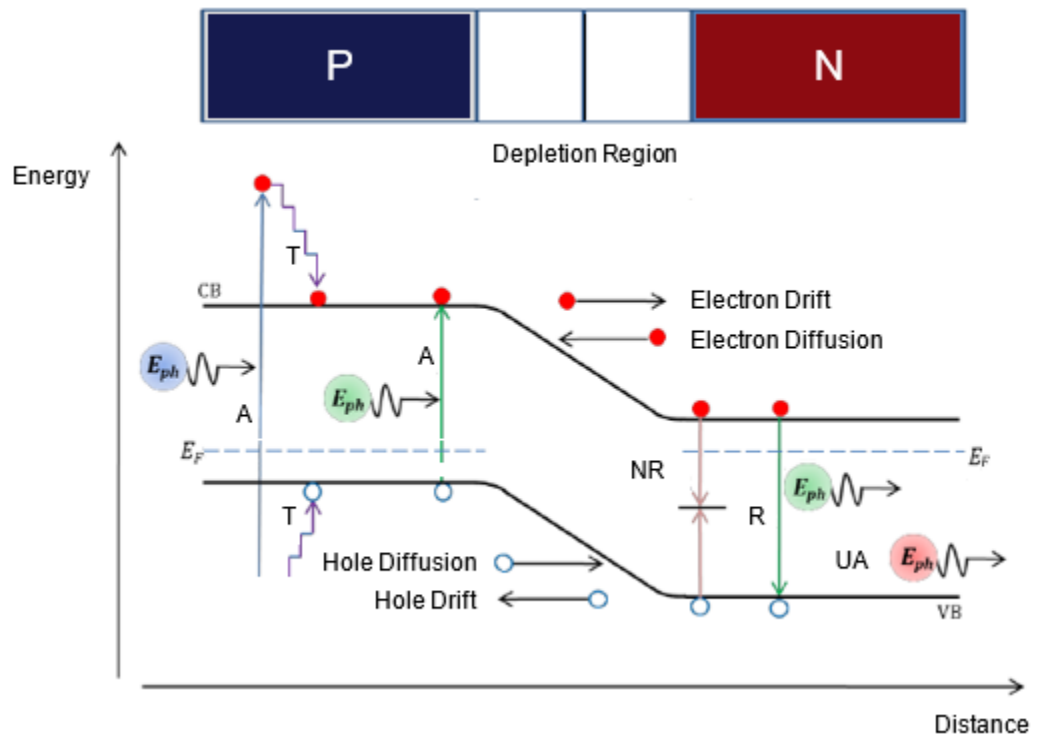
Figure 1.4 Schematic diagram of a p-n junction and a corresponding band diagram, showing the absorption (A), thermalisation (T), non-radiative recombination (NR), radiative recombination (R), unabsorbed radiation (UA).

1.4 Solar cell operation

The operation of a solar cell based on a p-n junction involve four main steps, namely, the generation of electron-hole pairs (EHP), the collection of the carriers driven by the built-in electric field in the depletion region, the voltage generation across the solar cell, and the dissipation of power in an external load. The generation of the photocurrent can be described as shown in Equation 1.4.

$$J_L = q \int_0^W G(x) CP(x)\, dx$$

(J_L: photocurrent density

W: thickness of the device

$CP(x)$: collection probability at x

x: depth into the material)

Equation 1.4

In a solar cell, the power is produced by generating both a voltage and a current. The former is generated by the photovoltaic effect, in which the collection of light-generated carriers causes electrons to move to the n-type side and holes to move to the p-type side. The light-generated current, of which the current density is J_L, the drift current that flows in the opposite direct to that of diffusion current of the diode. When the solar cell is under a short-circuit condition, the voltage across the solar cells is zero as there is no build-up of charge from the carriers exiting the device as photocurrent. On the other hand, when there is a load across the solar cell, electrons and the holes build up in the n-type and p-type region, respectively. This leads to a reduction in the net electric field across the p-n junction decreases, and hence, an increase in the diffusion diode current. The solar cell reaches an equilibrium where there is a voltage across the junction and a current

through the solar cell. The current is equal to the dark current subtracted

by the photocurrent, and the current density is given as Equation 1.5.

$$J_D = J_0 \left(e^{\frac{qV}{nkT}} - 1 \right) - J_L$$

<div align="right">**Equation 1.5**</div>

Therefore, the current density-voltage (J-V) characteristics of a solar cell

is the superposition of the dark current and the photocurrent [7], as shown

in Figure 1.5 (a). The superposed J-V curve move into the fourth quadrant,

where the power can be extracted. Figure 1.5 (b) shows the equivalent

circuit diagram of a solar cell, where the photocurrent and the radiative

recombination are represented by a current source and a rectifying diode,

respectively.

(a)
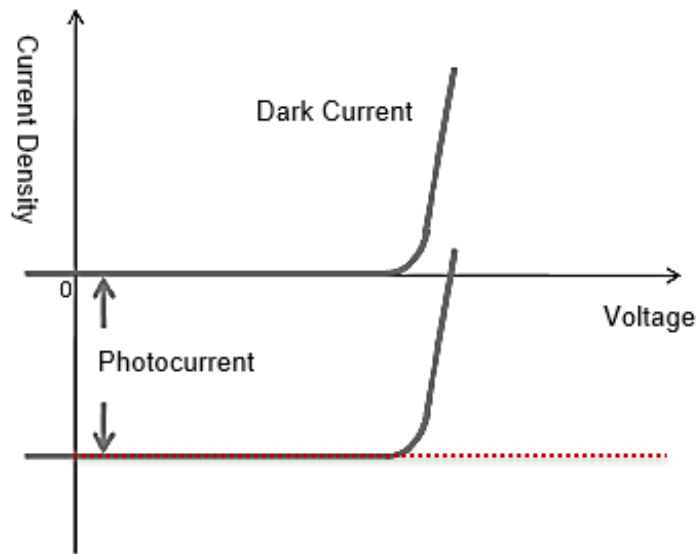
(b)
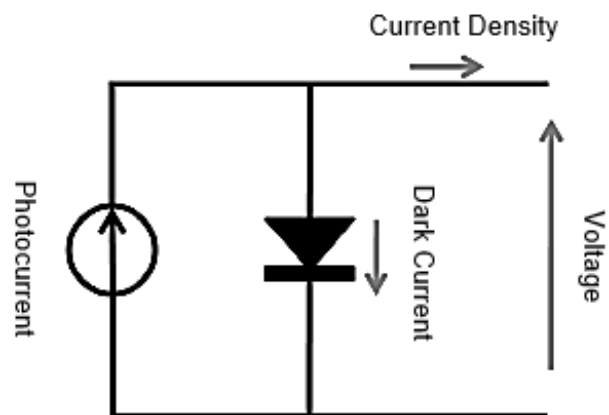
Figure 1.5 (a) Current density-voltage curves of a solar cell showing its photocurrent and dark current. (b) Equivalent circuit diagram of a solar cell.

1.5   Losses in solar cells

The non-ideal characteristics originate from the losses in the solar cell. The losses can be divided into the optical and electrical components, as shown in Figure 1.6. Two of the main losses in conventional solar cells are the sub-bandgap losses and lattice thermalisation. The former leads to a reduction in the current and the latter results in the reduction in the voltage. These two optical losses account for more than 50% of the losses in single bandgap solar cells [8]. Recombination losses can also cause a reduction in the output voltage.
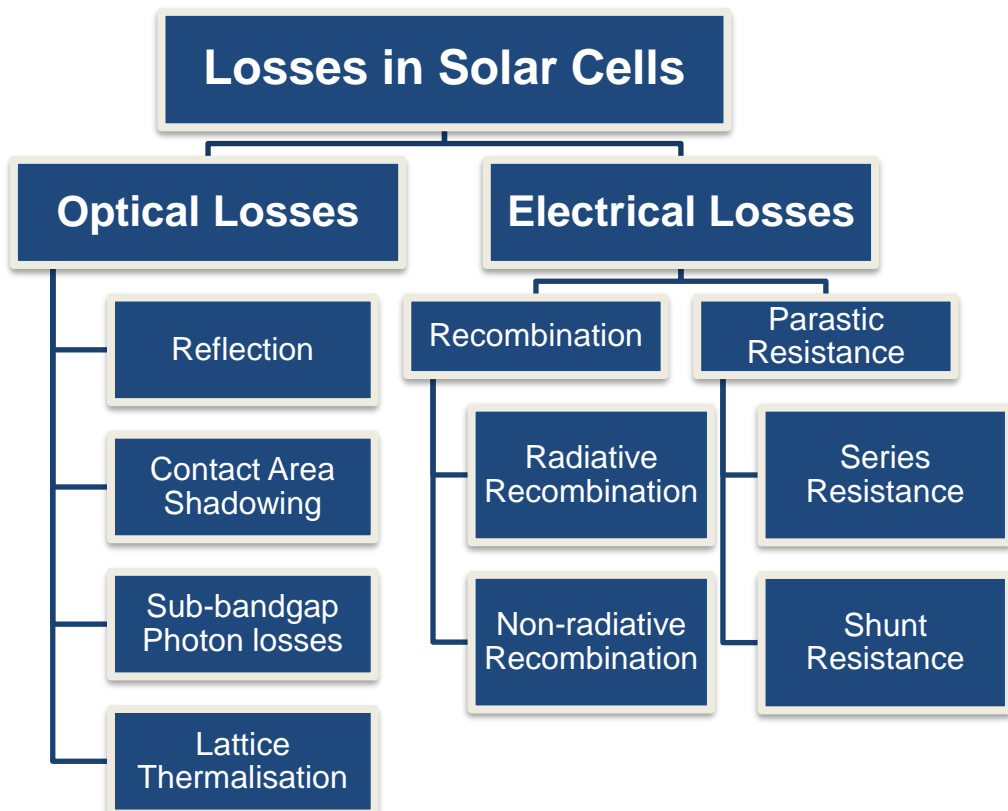
Figure 1.6 Types of losses in a solar cell.

1.6 Solar cell performance

1.6.1 Quantum efficiency

The quantum efficiency (QE) is the ratio of the number of carriers collected by a solar cell to the number of incident photons at a given wavelength. In an ideal solar cell, in which all photons at a particular wavelength are absorbed and all carriers are collected, the QE at that particular wavelength is equal to 1. In a real solar cell, the QE is decided by the absorbing properties and the carrier properties of the material. Typically, the QE is reduced by surface recombination at high-energy region, and by bulk recombination at low-energy region. Figure 1.7 shows the examples of QE spectra in ideal and real solar cells.
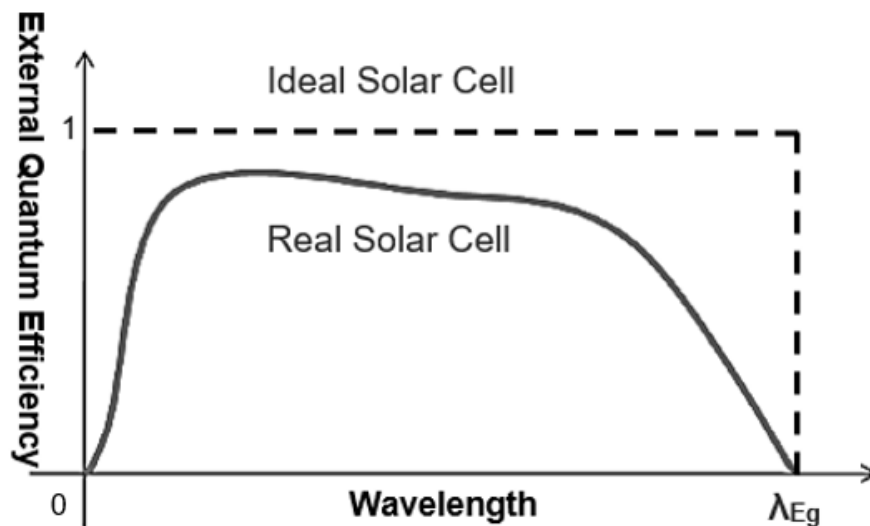
Figure 1.7 External quantum efficiency of an ideal solar cell and a real.

When calculating the external quantum efficiency (EQE) the transmission and reflection of a solar cell are taken into account, whereas the internal quantum efficiency (IQE) does not reflect the influence of them.

1.6.2 Current density-voltage characteristics

The current density-voltage (J-V) characteristics of a solar cell is the superposition of the dark current and the photocurrent [7]. Parameters, such as the short-circuit current density (J_{SC}), the open-circuit voltage (V_{OC}), the fill factor (FF) and the efficiency (η) can be extracted from the J-V curve. Conventionally, J-V curves for photovoltaics are inverted so that they are in the first quadrant, as shown in Figure 1.8.
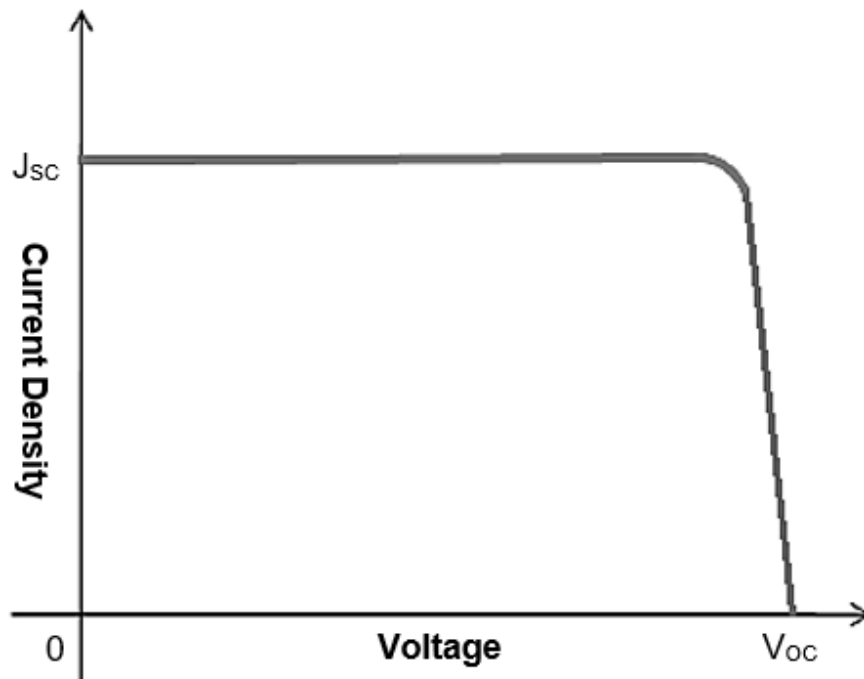
Figure 1.8 Current density-voltage characteristic of a solar cell showing the short-circuit current density (J_{SC}) and the open-circuit voltage (V_{OC}).

1.6.2.1 Short-circuit current density

The short-circuit current density (J_{SC}) is the maximum output current density of a solar cell, and is achieved when the voltage is equal to zero. J_{SC} depends on the QE, and the intensity and the spectrum of the incident light, as shown in Equation 1.6.

$$J_L = q \int_0^\infty F(\lambda)QE(\lambda)\, d\lambda$$

$(F(\lambda)$: photon flux (m^{-2}s^{-1}nm^{-1}))

Equation 1.6

In an ideal solar cell, J_{SC} is equal to the photocurrent.

1.6.2.2 Open-circuit voltage

The open-circuit voltage (V_{OC}) is the maximum output voltage of a solar cell, and is achieved when the current is equal to zero. V_{OC} depends on the J_{SC} and J_0. As J_{SC} typically remains relatively constant and J_0 can vary by several orders of magnitude, and J_0 depends on recombination, V_{OC} can be used as a measure of the recombination in a solar cell. The V_{OC} is given by Equation 1.7.

$$V_{oc} = \frac{nkT}{q} \ln\left(\frac{J_{sc}}{J_o} + 1\right)$$

Equation 1.7

1.6.2.3 Fill factor

The fill factor (FF) is the ratio of the product of the J_{SC} and V_{OC} to the product of the current density at the maximum power point (J_{mp}) and the voltage at the maximum point (V_{mp}).

$$FF = \frac{J_{mp}V_{mp}}{J_{sc}V_{oc}}$$

Equation 1.8
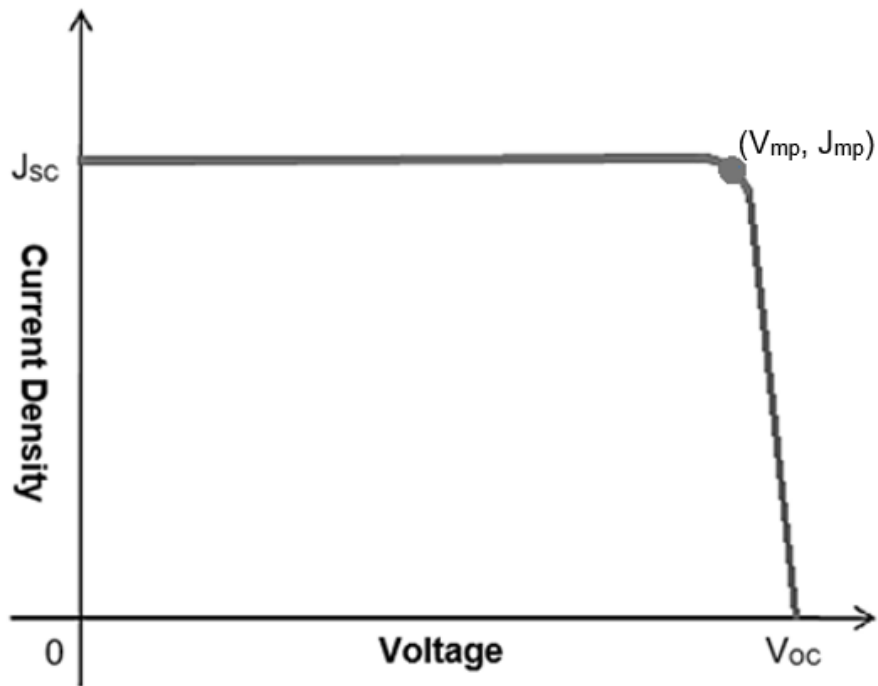
Figure 1.9 Current density-voltage characteristic of a solar cell showing the maximum power point.

As shown in Equation 1.8 and Figure 1.9, the FF is the area of the largest rectangle that can fit in the J-V curve, and can be used as a measure of the quality of the p-n junction and series resistance of a solar cell. The maximum power density (P_m) that can be extracted from a solar cell is given as Equation 1.9.

$$P_m = J_{sc}V_{oc}\,FF$$

<div align="right">**Equation 1.9**</div>

1.6.2.4 *Power conversion efficiency*

Power conversion efficiency (η) is the ratio of the output energy from a solar cell to the input incident solar energy. The standard measurement conditions for terrestrial solar cells are the AM1.5 Global solar spectrum at 25 °C. The efficiency can be described as Equation 1.10.

$$\eta = \frac{J_{sc}V_{oc}\,FF}{P_{IN}}$$

(P_{IN}: input power density (1000 Wm^{-2} under AM1.5 Global spectrum))

<div align="right">**Equation 1.10**</div>

The best efficiency achieved to date for a thin film GaAs solar cell under AM1.5 is 28.8 ± 0.9 % [9]. When semiconductor materials with low bandgap are used for a solar cell, more low energy photons can be absorbed, which leads to an increase in the current density. However, this will also lead to an increase in the dark current., as shown in Equation 1.11, and in turn decrease the open-circuit voltage.

$$J_0 \propto e^{-\frac{E_g}{kT}}$$

Equation 1.11

On the other hand, solar cells with a high bandgap exhibit a low J_{SC} as photons with lower energy than the bandgap are not absorbed. However, the V_{OC} will be greater due to a lower dark current. Therefore, there is an optimal bandgap energy at which the current density and open-circuit voltage give the highest efficiency. Figure 1.10 shows the maximum theoretical efficiency of single-bandgap solar cells as a function of bandgap energy under AM1.5 Global spectrum. The maximum efficiency is achieved at ~ 1.37 eV which is close to that of GaAs (~ 1.42 eV).
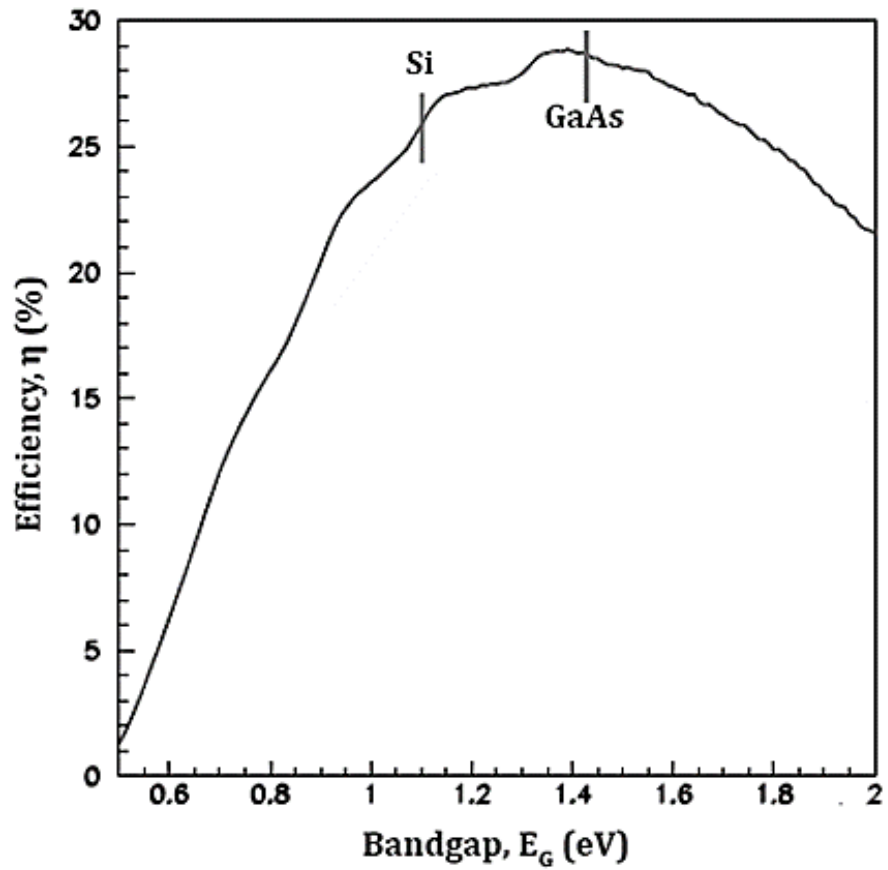
Figure 1.10 Limiting efficiency for single bandgap solar cells as a function of bandgap under the AM1.5 global spectrum (adapted from [10]).

1.6.3 Parasitic resistances

Typically, the efficiency of a solar cell is reduced due to the dissipation of the power across the internal resistances during the operation. These parasitic resistances are the series and shunt resistances. Figure 1.11 shows the equivalent circuit diagram of a solar cell with parasitic resistances.
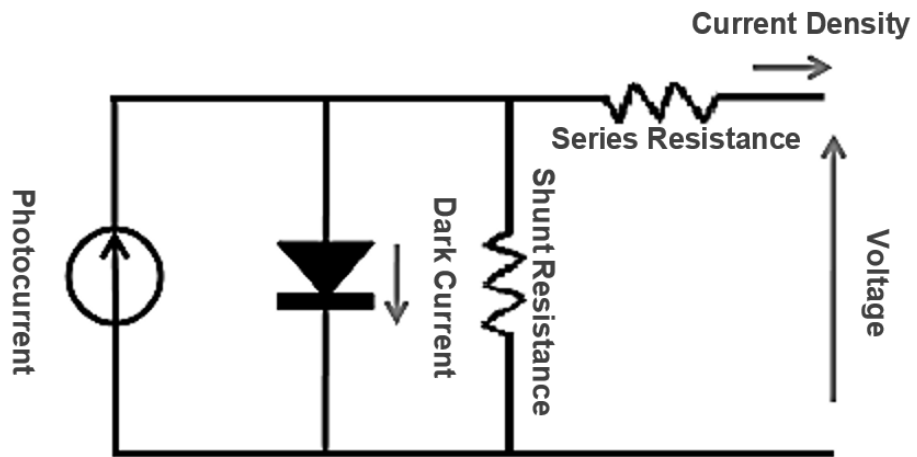
Figure 1.11 Equivalent circuit diagram of a solar cell showing parasitic resistances.

1.6.3.1 Series resistance

The series resistance, RS, originates from the bulk resistance of the semiconductor material, the resistance of the metal contacts, and the resistance between the metal contacts and the semiconductor material. In an ideal solar cell, the series resistance is equal to zero. However, in a real solar cell, the fill factor, and hence the efficiency, decrease as the series resistance increases. If the series resistance is too high, the current density can also be reduced. However, the open-circuit voltage remains unaffected as under the open-circuit condition there is no current through the solar cell. The series resistance can be estimated by calculating the slope of the J-V curve around the open-circuit voltage. Figure 1.12 shows the effects of the series resistance on the J-V curve.
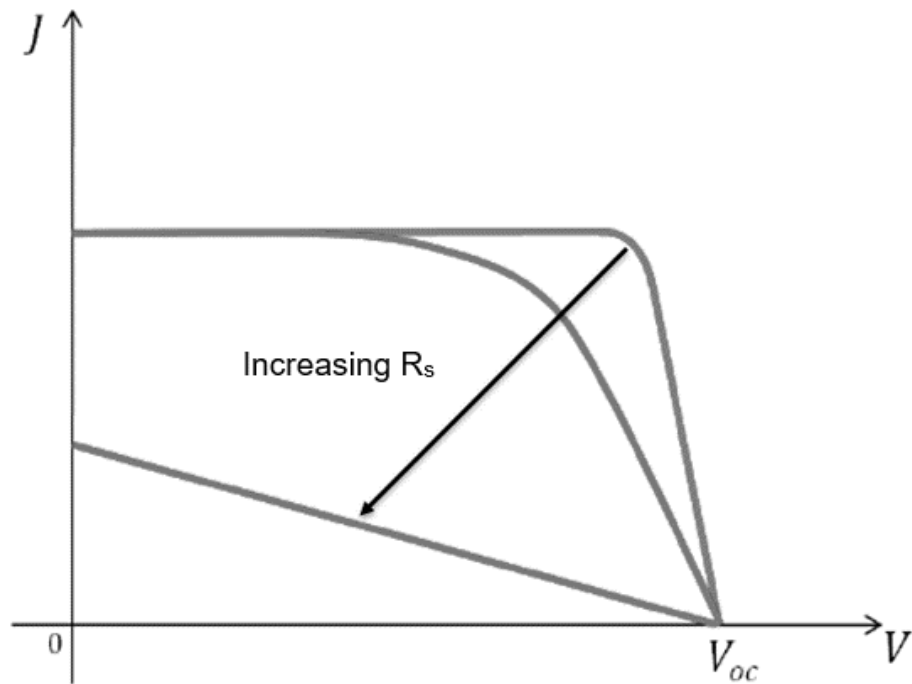
Figure 1.12 J-V characteristics showing the effects of series resistance.

1.6.3.2 Shunt resistance

The shunt resistance, R_{SH}, is mainly caused by fabrication defects, such as the partial shorting across the p-n junction of the solar cell. The partial shorting typically occurs near the edge of the solar cell, which create alternative paths for the photocurrent. Therefore, the current through the solar cell is reduced, and hence the voltage across the solar cell is also reduced. The short-circuit current is not affected by the shunt resistance. Figure 1.13 shows the effects of the series resistance on the J-V curve.
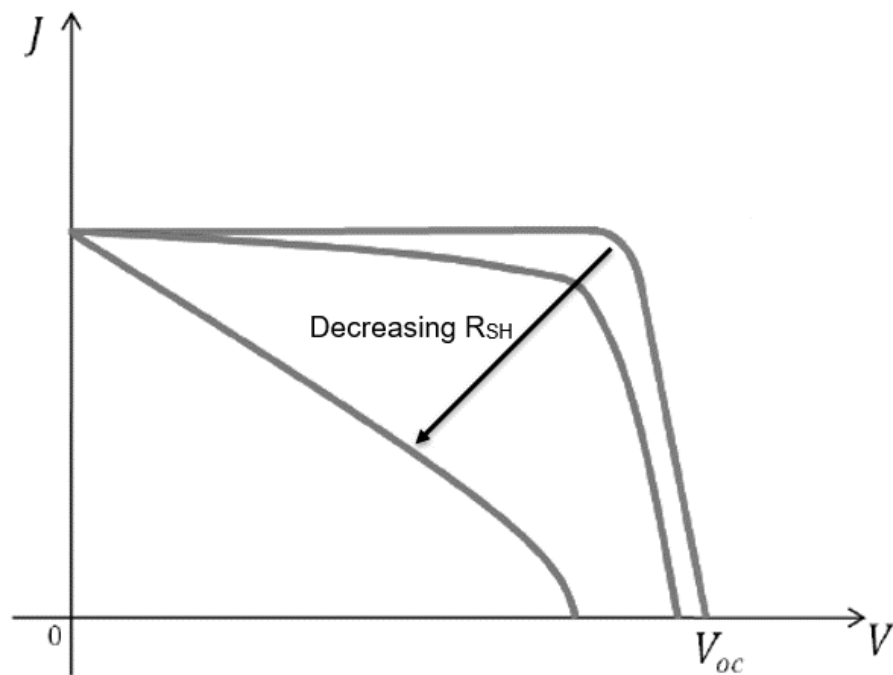
Figure 1.13 J-V characteristics showing the effects of shunt resistance.

By taking the series resistance and shunt resistance into account, the current density-voltage characteristics can be described as Equation 1.12.

$$J = J_L - J_0 \left(e^{\frac{qV}{nkT}} - 1 \right) - \frac{V + JR_SA}{R_{SH}}$$

(A: solar cell area that is exposed to the light)

Equation 1.12

1.6.4 Temperature and light intensity

During the operation, the power conversion efficiency of a solar cell is influenced by the cell temperature. Higher temperature leads to a reduction of the bandgap energy, and hence an increase in the short-circuit current density. However, the increase in the short-circuit current density is usually undermined by the significant drop in the open-circuit voltage. Solar cell performances also depend on the intensity of the incident light. The short-circuit current density is proportional to the intensity of the incident light, and the open-circuit voltage is logarithmically dependent on the short-circuit current, as shown in Equation 1.13.

$$V_{oc} = \frac{nkT}{q} \ln \left(\frac{XJ_{sc}}{J_o} + 1 \right)$$

(X: concentration of the incident light (1 sun refers to AM1.5 illumination.))

Equation 1.13

The increase in the efficiency from high concentration is reduced by parasitic resistance losses and the high cell temperature.

1.6.5 Solar cell structures

Due to optical losses, recombination, and physical constraints the performance of solar cells is limited. Equation 1.14 and Figure 1.14 give more realistic descriptions of the current produced by a solar cell by taking the non-radiative recombination and parasitic resistances into account.

$$J = J_L - J_{01}\left(e^{\frac{qV}{kT}} - 1\right) - J_{02}\left(e^{\frac{qV}{2kT}} - 1\right) - \frac{V + JR_SA}{R_{SH}}$$

(J_{01}: dark saturation currents for the radiative current

J_{02}: dark saturation currents for the non-radiative current)

Equation 1.14
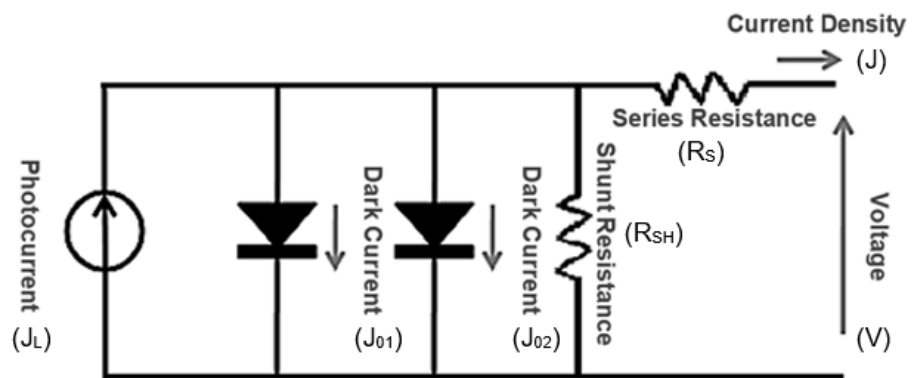
Figure 1.14 Equivalent circuit diagram of a realistic solar cell

Therefore, there is a need for engineering the solar structure in order to minimise the optical and recombination losses.

1.6.5.1 Window layer

Recombination at the front surface of a solar cell can have a significant impact on its performance. This is because surfaces and interfaces typically have a large number of recombination centres due to the abrupt termination of the crystal lattice. In order to prevent this, a thin layer of high bandgap material, referred to as the window layer, is introduced at the front surface to create a barrier. Therefore, the minority carriers can be repelled towards the depletion region, and can be collected to contribute to the power generation of the solar cell. For III-V solar cells, AlGaAs or AlInP is often used as a window layer. Usually, a window layer is covered with a capping layer in order to prevent oxidation. For a low-resistance contact, a capping layer is highly doped.

1.6.5.2 Back surface fields

The back surface fields (BSF), which is introduced at the base of a solar cell, has a similar function to the window layer. Minority carriers are bounced back towards the depletion region to aid the carrier collection. BSF can be implemented by high doping or by using high bandgap materials, such as AlGaAs or GaInP.

1.6.5.3 Metal contacts

Light-generated current from a solar cell is extracted through the metal contacts on the front and back surfaces. Unlike the back surface, the front surface not only needs a metal contact for the current to be collected, but also needs to be exposed to the incident light. Therefore, when designing the metal contact for the front surface, the shadow area, as well as the series resistance of the metal contact, needs to be taken into consideration. It has been demonstrated that using tapered fingers for the metal contacts can lower the losses [11]. Metal contacts can be fabricated using a shadow mask or photolithography with a combination of metals, including Au, Ge, Ni, Zn, and Ti.

1.6.5.4 Anti-reflection coating

In order to reduce the loss from the reflection at the surface, an anti-reflection (AR) coating can be employed. For instance, bare Si has a surface reflection of over 30 % [12]. The reflection can be reduced by surface texturing and by applying AR coating [13]. AR coatings on solar cells typically consist of a thin layer of dielectric materials, such as Si_3N_4 and MgF_2.

1.7 Multi-junction solar cells

Multi-junction solar cells (MJSCs), which are also known as tandem cells, are the highest performing class of solar cells in terms of efficiency [9]. They are composed of multiple semiconductor diodes with different bandgaps connected in series. In most MJSC, the cell with the largest bandgap is placed at the top and the cell with the smallest bandgap is placed at the bottom. In this manner, they can selectively absorb different parts of the solar spectrum, and achieve a fundamental efficiency advantage over single-junction solar cells (SJSCs). MJSCs were first developed for space applications, however, they can be of use and cost-effective for terrestrial applications when used with concentrator photovoltaic (CPV) systems [14]. Commercially, triple junction solar cells are available with efficiencies over 40 %, and research is now proceeding towards quad-junction and five-junction structures, with new records for efficiency under concentration [15] and at one sun [16].

1.8 Nanowire solar cells

Two of the major factors that can increase the difficulty and the cost of solar cell (SC) fabrication are the lattice mismatch and thermal expansion coefficient mismatch between different semiconductor materials. One of the possible solutions to this is to use nanowire (NW) structures for SCs. NW structures can facilitate strains due to lattice mismatch and thermal

expansion coefficient mismatch owing to their small lateral cross-section area. Yoshimura *et al.* reported the growth of 90 nm InGaAs NWs with a lattice mismatch of 2.1 % relative to the GaAs substrate without defects. Therefore, III-V materials can be combined with low-cost substrates.

There are also many advantages of using NWs in terms of solar cell performances. NWs have one-dimensional structures with subwavelength diameters and high refractive index. Therefore, NWs can have a significantly larger absorption cross-section for their physical size [17]. In addition, wavelength-tunability can be achieved by varying the dimensions of NWs [18]–[20], which means that tailoring the absorption spectrum involves fewer difficulties. Using NWs in a SC can also be beneficial for photon management. An array with high-density NWs can function as a refractive index transition layer, which can significantly reduce the light reflectance [21], [22]. Furthermore, NWs with subwavelength dimensions can enhance light scattering effect [23], [24]. This leads to the elongated light propagation path in the solar cell. Garnett *et al.* have shown that the light propagation path in NW arrays can be ~ 73 times longer compared with their physical thickness [25].

1.9   Intermediate band solar cells

One of the major losses in single bandgap solar cell are the sub-bandgap photon losses. In other words, photons with lower energies than the bandgap of the solar cell material will not be utilised in power generation. Therefore, in order to improve the efficiencies of solar cells, it is necessary to harness the low-energy photons. The concept of the intermediate band solar cell (IBSC) was first proposed in 1997 by A. Luque and A. Martí [26]. The IBSC utilises a collection of intermediate levels within the bandgap, called the intermediate band (IB), to absorb sub-bandgap energy photons. Its potential to exceed the Shockley-Queisser limit of 31 % [27], and reach the theoretical limit of 63.2 % [28] arises from the additional photocurrent generated by the sub-bandgap photon absorption. In an IBSC, the IB is formed within the bandgap of a semiconductor and functions as a stepping-stone to assist electrons to be transferred from the VB to the CB. In this way, in addition to the photon absorption by electron transitions between the VB and the CB, the absorption of sub-bandgap photons can be realised via IB, which in turn increases the absorption range of the solar cell in the solar spectrum. Figure 1.15 and Figure 1.16 illustrates the concept of the IBSC and the corresponding band diagram, respectively.
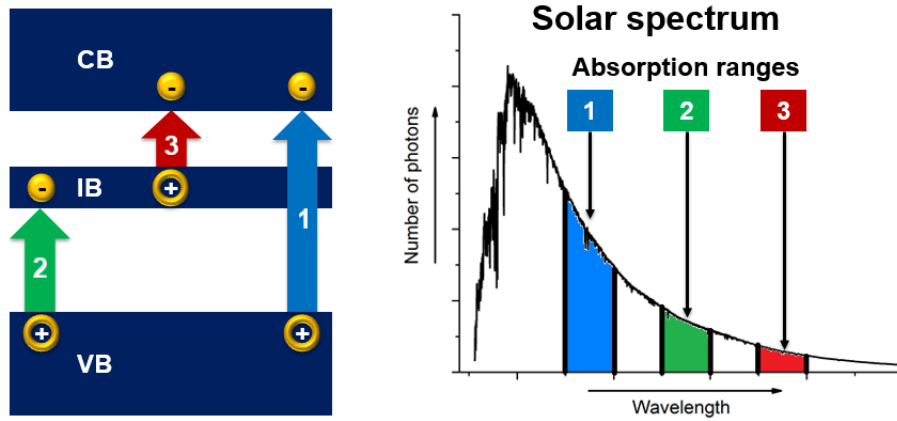
Figure 1.15 Electron transitions in an intermediate band solar cell (left) and corresponding photons absorption range of solar spectrum
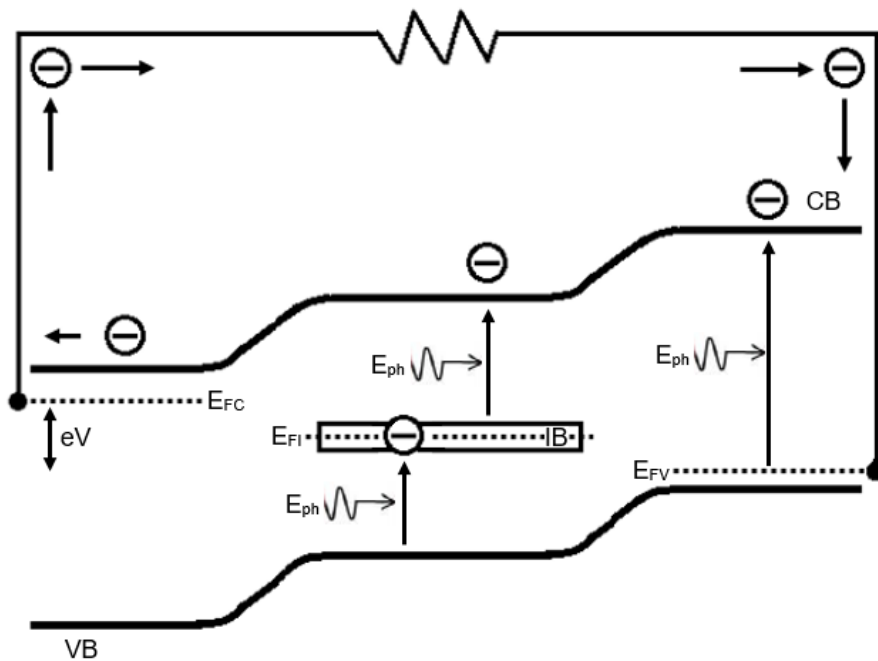
Figure 1.16 Band diagram showing the photon absorption in an intermediate band solar cell.

An IBSC can be made by sandwiching an IB material between conventional p-type and n-type semiconductor materials. The doped semiconductor materials act as selective contacts for electrons and holes, and prevent the IB from contacting the external electrodes. As the process of interband carrier relaxation is slower than that within a band, a distinct quasi-Fermi level is associated with each band: E_{FC}, E_{FV}, and E_{FI}. Since the output voltage eV is given by the difference between the quasi Fermi levels of electrons and holes, the voltage is still limited by the total bandgap. [29]. In order to achieve an improvement in the power conversion efficiency, the increase in the photocurrent by the increased photon absorptions should not accompany a reduction in the output voltage.

1.9.1   Quantum dot intermediate band solar cells

Since the concept of the IBSC was proposed in 1997, significant efforts have been made to realise IBSCs with efficiencies that exceed the Shockley-Queisser limit of 31 % [27]. One of the candidates for the high-efficiency IBSC is the quantum dot intermediate band solar cell (QD-IBSC). In a QD-IBSC, the QDs are embedded in a barrier material with a higher bandgap, and placed in the intrinsic region of the p-i-n structure. QDs are nanoscale clusters of semiconductor material with three-dimensional confinement. Unlike other low-dimensional structures, such as quantum wells or nanowires, QDs have a discrete density of states due to their three-

dimensional confinement [30]. This enables QDs to create a zero density of states between the IB and the CB, supporting the formation of individual quasi-Fermi levels [31]. The operation of QD-IBSCs have been demonstrated using material systems, such as In(GaAs)/GaAs [32], [33], InAs/GaNAs [34], and GaSb/GaAs [35]. Figure 1.17 shows the simplified band diagram of a QD-IBSC.
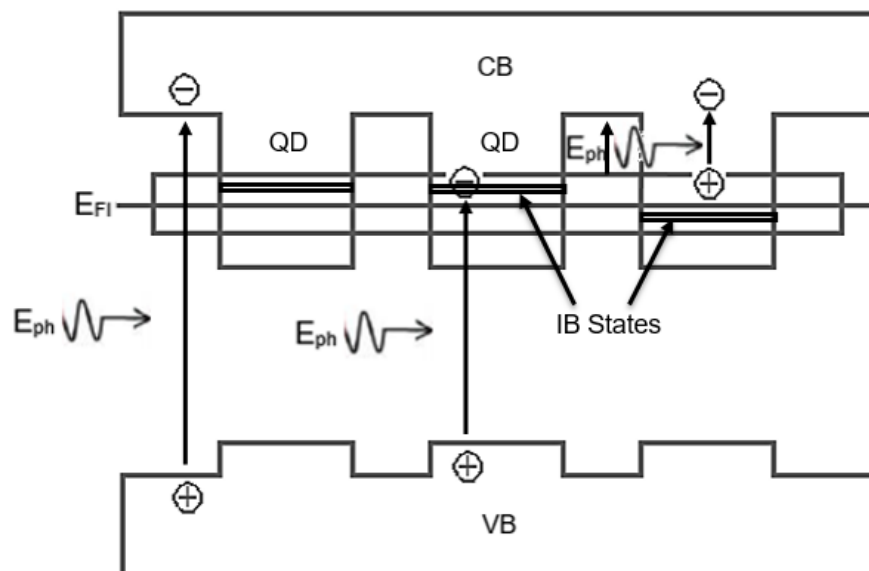
Figure 1.17 Simplified band diagram showing the photon absorption in an quantum dot intermediate band solar cell.

1.9.1.1 Requirements and challenges

However, over the last decade, several challenges in implementing high-efficiency QD-IBSCs have been identified.

1.9.1.1.1 Quantum dot arrays with high density and uniformity

In order to achieve high absorption from QDs, and to ensure that the wavefunctions of QDs form a band as opposed to localised energy levels, QD-IBSCs needs to have QD arrays with high-density and uniformity. Solar cell performances depend significantly on the uniformity of dots. Poor uniformity in the QD size will lead to a collection of multilevels instead of an IB [36]. The tolerance limit of size dispersion of QDs in an IB-QDSC is estimated to be be ~ 10 % [37].

1.9.1.1.2 Thermal decoupling between intermediate band and conduction band

Thermal coupling between the IB and CB enables the carriers to be thermally excited or relaxed between the IB and the CB [29], [38], [39]. This thermal process suppresses the second-photon absorption and lowers the effective bandgap energy of the SC leading to a reduced open-circuit voltage (Voc) [32], [40]. Tutu *et al.* demonstrated suppression of thermal escape of electrons in QDs by suppressing the formation of the WL via AlAs cap layer (CL) deposition [41]. Whereas Lam *et al.* reported reduced thermal coupling between the WL and QD states by introducing a potential barrier at the QD/WL interface via Si doping [42].

1.9.1.1.3 Strain balancing

The accumulated strain from the QDs leads to the formation of threading dislocations [43]–[45]. The strain-induced dislocations across the QD region result in a short minority carrier lifetime, and hinders the stacking of QD layers that are needed to maximise the QD photon absorption [44]–[47]. Studies have shown that strain-induced dislocations can be minimised using a high-growth temperature GaAs spacer layer that separates each QD layer [43], [44]. Yang *et al.* demonstrated saturation of strain-induced dislocations in InAs QDs using Si doping [46].

1.9.1.1.4 Partial filling of intermediate band

The performance of IBSCs relies on an IB that is partially filled with electrons [31], [48]. For strong sub-bandgap photon absorption, the IB needs to have empty states to receive the electrons pumped from the VB, and states filled with electrons to pump electrons to the CB. Luque *et al.* proposed the use of doping as a method to achieve partial filling of the confined states in the IB [49]. It has also been demonstrated, by Martí *et al.* [50], that half-filling of the IB can be realised by doping the capping layers of QDs with Si in InAs/(Al, Ga)As quantum dot solar cells (QDSCs).

1.10 Thesis structure

This thesis describes the development of high-efficiency QD IBSCs based on III-V QD material systems. The project involves the design, epitaxial growth, fabrication and characterisation of solar cells. Epitaxial growth is performed using molecular beam epitaxy (MBE).

Chapter 1 presents a theoretical background to solar energy and physics of solar cells, along with an overview of different types of solar cells.

Chapter 2 discusses the experimental methods involved in this project. The chapter begins with an introduction to MBE growth, followed by discussion of III-V material processing and solar cell fabrication.

Chapter 3 investigates the influence of Si doping on InAs/GaAs quantum dot solar cells with AlAs cap layer. A voltage recovery and state filling are achieved with moderate Si doping density, which holds some promise for overcoming some of the main challenges in implementing quantum dot intermediate band solar cells with the efficiencies close to that of the theoretical model.

InAs-QD/GaAs$_{1-x}$Sb$_x$-QW SCs with a GaAs interlayer with four Sb compositions are studied in Chapter 4. Enhanced type-II characteristics are observed from these solar cells.

The influence of different doping methods and methods are discussed in Chapter 5. The results show a clear relationship between the degree of

separation between the Si dopants and the QDs achieved by different doping methods, and the number of non-radiative recombination.

Finally, chapter 6 highlights the conclusions from the findings presented in this thesis, examines ongoing work and offers suggestions for future research.

1.11 References

[1]   R. Hulstrom, *Solar Resources*. MIT Press, 1989.

[2]   D. J. C. MacKay, *Sustainable Energy--without the Hot Air*. UIT, 2009.

[3]   J. Nelson, *The Physics of Solar Cells*. Imperial College Press, 2003.

[4]   Solar energy - Reference solar spectral irradiance at the ground at different receiving conditions - Part 1: Direct normal and hemispherical solar irradiance for air mass 1.5, ISO 9845-1:1992, 1992.

[5]   S. O. Kasap, *Optoelectronic devices and photonics: principles and practices*. 2000.

[6]   W. Shockley, 'The Theory of p-n Junctions in Semiconductors and p-n Junction Transistors', *Bell Syst. Tech. J.*, vol. 28, no. 3, pp. 435–489, Jul. 1949.

[7]   F. A. Lindholm, J. G. Fossum, and E. L. Burgess, 'Application of the superposition principle to solar-cell analysis', *IEEE Trans. Electron Devices*, vol. 26, no. 3, pp. 165–171, Mar. 1979.

[8]   L. C. Hirst and N. J. Ekins-Daukes, 'Fundamental losses in solar cells', *Prog. Photovolt. Res. Appl.*, vol. 19, no. 3, pp. 286–293, May 2011.

[9]   M. A. Green, K. Emery, Y. Hishikawa, W. Warta, and E. D. Dunlop, 'Solar cell efficiency tables (version 47)', *Prog. Photovolt. Res. Appl.*, vol. 24, no. 1, pp. 3–11, Jan. 2016.

[10] N. J. Ekins-Daukes, *An investigation into the efficiency enhancement of strained and strain-balanced quantum well solar cells*. University of London, 2000.

[11] S. R. Wenham, M. A. Green, M. E. Watt, and R. Corkish, *Applied Photovoltaics*. STYLUS PUB LLC, 2007.

[12] M. A. Green, 'Self-consistent optical parameters of intrinsic silicon at 300 K including temperature coefficients', *Sol. Energy Mater. Sol. Cells*, vol. 92, no. 11, pp. 1305–1310, Nov. 2008.

[13] G. Bauer, 'Absolutwerte der optischen Absorptionskonstanten von Alkalihalogenidkristallen im Gebiet ihrer ultravioletten Eigenfrequenzen', *Ann. Phys.*, vol. 411, no. 4, pp. 434–464, 1934.

[14] R. McConnell and V. Fthenakis, 'Concentrated Photovoltaics', in *Third Generation Photovoltaics*, V. Fthenakis, Ed. InTech, 2012.

[15] F. Dimroth *et al.*, 'Wafer bonded four-junction GaInP/GaAs//GaInAsP/GaInAs concentrator solar cells with 44.7% efficiency', *Prog. Photovolt. Res. Appl.*, vol. 22, no. 3, pp. 277–282, Mar. 2014.

[16] E. M. Rehder *et al.*, 'Environmental testing of inverted metamorphic solar cells for space', in *2014 IEEE 40th Photovoltaic Specialist Conference (PVSC)*, 2014, pp. 3608–3611.

[17] L. Cao, J. S. White, J.-S. Park, J. A. Schuller, B. M. Clemens, and M. L. Brongersma, 'Engineering light absorption in semiconductor nanowire devices', *Nat. Mater.*, vol. 8, no. 8, pp. 643–647, Aug. 2009.

[18] P. M. Wu, N. Anttu, H. Q. Xu, L. Samuelson, and M.-E. Pistol, 'Colorful InAs Nanowire Arrays: From Strong to Weak Absorption with Geometrical Tuning', *Nano Lett.*, vol. 12, no. 4, pp. 1990–1995, Apr. 2012.

[19] Y.-A. Dai *et al.,* 'Subwavelength Si nanowire arrays for self-cleaning antireflection coatings', *J. Mater. Chem.*, vol. 20, no. 48, pp. 10924–10930, Nov. 2010.

[20] S. L. Diedenhofen, O. T. A. Janssen, G. Grzela, E. P. A. M. Bakkers, and J. Gómez Rivas, 'Strong geometrical dependence of the absorption of light in arrays of semiconductor nanowires', *ACS Nano*, vol. 5, no. 3, pp. 2316–2323, Mar. 2011.

[21] L. Hu and G. Chen, 'Analysis of Optical Absorption in Silicon Nanowire Arrays for Photovoltaic Applications', *Nano Lett.*, vol. 7, no. 11, pp. 3249–3252, Nov. 2007.

[22] J. Zhu, C.-M. Hsu, Z. Yu, S. Fan, and Y. Cui, 'Nanodome Solar Cells with Efficient Light Management and Self-Cleaning', *Nano Lett.*, vol. 10, no. 6, pp. 1979–1984, Jun. 2010.

[23] O. L. Muskens *et al.*, 'Large Photonic Strength of Highly Tunable Resonant Nanowire Materials', *Nano Lett.*, vol. 9, no. 3, pp. 930–934, Mar. 2009.

[24] T. Strudley, T. Zehender, C. Blejean, E. P. A. M. Bakkers, and O. L. Muskens, 'Mesoscopic light transport by very strong collective multiple scattering in nanowire mats', *Nat. Photonics*, vol. 7, no. 5, pp. 413–418, May 2013.

[25] E. Garnett and P. Yang, 'Light Trapping in Silicon Nanowire Solar Cells', *Nano Lett.*, vol. 10, no. 3, pp. 1082–1087, Mar. 2010.

[26] A. Luque and A. Martí, 'Increasing the Efficiency of Ideal Solar Cells by Photon Induced Transitions at Intermediate Levels', *Phys. Rev. Lett.*, vol. 78, no. 26, pp. 5014–5017, Jun. 1997.

[27] W. Shockley and H. J. Queisser, 'Detailed Balance Limit of Efficiency of p-n Junction Solar Cells', *J. Appl. Phys.*, vol. 32, no. 3, pp. 510–519, Mar. 1961.

[28] A. Luque, A. Martí, and C. Stanley, 'Understanding intermediate-band solar cells', *Nat. Photonics*, vol. 6, no. 3, pp. 146–152, Mar. 2012.

[29] A. Luque and A. Martí, 'The Intermediate Band Solar Cell: Progress Toward the Realization of an Attractive Concept', *Adv. Mater.*, vol. 22, no. 2, pp. 160–174, Nov. 2010.

[30] A. Zrenner, 'A close look on single quantum dots', *J. Chem. Phys.*, vol. 112, no. 18, pp. 7790–7798, May 2000.

[31] A. Martí, L. Cuadra, and A. Luque, 'Partial filling of a quantum dot intermediate band for solar cells', *IEEE Trans. Electron Devices*, vol. 48, no. 10, pp. 2394–2399, Oct. 2001.

[32] C. G. Bailey, D. V. Forbes, R. P. Raffaelle, and S. M. Hubbard, 'Near 1 V open circuit voltage InAs/GaAs quantum dot solar cells', *Appl. Phys. Lett.*, vol. 98, no. 16, p. 163105, Apr. 2011.

[33] K. A. Sablon, J. W. Little, V. Mitin, A. Sergeev, N. Vagidov, and K. Reinhardt, 'Strong Enhancement of Solar Cell Efficiency Due to Quantum Dots with Built-In Charge', *Nano Lett.*, vol. 11, no. 6, pp. 2311–2317, 2011.

[34] R. Oshima, A. Takata, and Y. Okada, 'Strain-compensated InAs/GaNAs quantum dots for use in high-efficiency solar cells', *Appl. Phys. Lett.*, vol. 93, no. 8, p. 083111, Aug. 2008.

[35] R. B. Laghumavarapu *et al.*, 'GaSb/InGaAs quantum dot–well hybrid structure active regions in solar cells', *Sol. Energy Mater. Sol. Cells*, vol. 114, pp. 165–171, Jul. 2013.

[36] S. Tomić, T. S. Jones, and N. M. Harrison, 'Absorption characteristics of a quantum dot array induced intermediate band: Implications for solar cell design', *Appl. Phys. Lett.*, vol. 93, no. 26, p. 263105, Dec. 2008.

[37] A. Martí, L. Cuadra, and A. Luque, 'Design constraints of the quantum-dot intermediate band solar cell', *Phys. E Low-Dimens. Syst. Nanostructures*, vol. 14, no. 1–2, pp. 150–157, Apr. 2002.

[38] S. Sanguinetti, M. Henini, M. Grassi Alessi, M. Capizzi, P. Frigeri, and S. Franchi, 'Carrier thermal escape and retrapping in self-assembled quantum dots', *Phys. Rev. B*, vol. 60, no. 11, pp. 8276–8283, Sep. 1999.

[39] E. Antolín *et al.*, 'Reducing carrier escape in the InAs/GaAs quantum dot intermediate band solar cell', *J. Appl. Phys.*, vol. 108, no. 6, p. 064513, Sep. 2010.

[40] A. Mellor, A. Luque, I. Tobías, and A. Martí, 'Realistic Detailed Balance Study of the Quantum Efficiency of Quantum Dot Solar Cells', *Adv. Funct. Mater.*, vol. 24, no. 3, pp. 339–345, Jan. 2014.

[41] F. K. Tutu *et al.*, 'InAs/GaAs quantum dot solar cell with an AlAs cap layer', *Appl. Phys. Lett.*, vol. 102, no. 16, p. 163907, Apr. 2013.

[42] P. Lam *et al.*, 'Voltage recovery in charged InAs/GaAs quantum dot solar cells', *Nano Energy*, vol. 6, pp. 159–166, May 2014.

[43] H. Y. Liu *et al.*, 'Improved performance of 1.3µm multilayer InAs quantum-dot lasers using a high-growth-temperature GaAs spacer layer', *Appl. Phys. Lett.*, vol. 85, no. 5, pp. 704–706, Aug. 2004.

[44] F. K. Tutu *et al.*, 'Improved performance of multilayer InAs/GaAs quantum-dot solar cells using a high-growth-temperature GaAs spacer layer', *J. Appl. Phys.*, vol. 111, no. 4, p. 046101, Feb. 2012.

[45] A. Martí *et al.*, 'Emitter degradation in quantum dot intermediate band solar cells', *Appl. Phys. Lett.*, vol. 90, no. 23, p. 233510, Jun. 2007.

[46] X. Yang *et al.*, 'Improved efficiency of InAs/GaAs quantum dots solar cells by Si-doping', *Sol. Energy Mater. Sol. Cells*, vol. 113, pp. 144–147, Jun. 2013.

[47] T. Sugaya, Y. Kamikawa, S. Furue, T. Amano, M. Mori, and S. Niki, 'Multi-stacked quantum dot solar cells fabricated by intermittent deposition of InGaAs', *Sol. Energy Mater. Sol. Cells*, vol. 95, no. 1, pp. 163–166, Jan. 2011.

[48] A. Martí *et al.*, 'Novel semiconductor solar cell structures: The quantum dot intermediate band solar cell', *Thin Solid Films*, vol. 511–512, pp. 638–644, Jul. 2006.

[49] A. Luque and A. Martí, 'A metallic intermediate band high efficiency solar cell', *Prog. Photovolt. Res. Appl.*, vol. 9, no. 2, pp. 73–86, Mar. 2001.

[50] A. Martí *et al.*, 'Production of Photocurrent due to Intermediate-to-Conduction-Band Transitions: A Demonstration of a Key Operating Principle of the Intermediate-Band Solar Cell', *Phys. Rev. Lett.*, vol. 97, no. 24, p. 247701, Dec. 2006.

Chapter 2
Epitaxial growth and fabrication of solar cells

The tasks involved in this research project include epitaxial growth, device processing and characterisation. The epitaxial structures in this work were designed and grown at the Department of Electronic and Electrical Engineering, University College London, using the Veeco Gen930 solid-source molecular beam epitaxy facility. Solar cell devices were processed at the London Centre for Nanotechnology. This chapter outlines the epitaxial growth and fabrication process associated with the project.

2.1 Epitaxial growth

Epitaxy is a process in which the formation of a crystalline overlayer occurs on a substrate. The term 'epitaxy' (Greek: 'epi': 'above' and 'taxis': 'in ordered manner') describes an ordered crystalline growth [1]. Two main epitaxial growth techniques used to produce high-quality III-V compound heterostructures are the metal-organic vapour phase epitaxy (MOVPE) and

molecular beam epitaxy (MBE). The difference between the two lies mainly in the deposition method. In MBE, the materials are grown on the substrate as they are delivered under ultra-high vacuum, whereas in MOVPE, the growth materials are delivered by gas phase and surface chemical reactions under moderate vacuum pressures. Despite the relatively slower growth rate, MBE has advantages over MOVPE in terms of the precision, and the ability to apply in situ surface analytical techniques to monitor the growth process in real-time.

2.2   Molecular beam epitaxy

MBE is an ultra-high vacuum epitaxial growth technique that operates by beaming atoms and molecules onto a heated crystalline substrate surface [2]–[4]. A significant development in III-V compound semiconductor growth by MBE were attained by A. Y. Cho and J. R. Arthur at Nokia Bell Telephone Laboratories (formerly named AT&T Bell Laboratories, Bell Telephone Laboratories and Bell Labs). Variations of MBE have been developed, such as the Gas-Source MBE, which uses hydrides, such as, arsine (AsH_3) as a group-V source, and metal-organic MBE which uses metal-organic compounds such as triethylgallium (TEGa) as a group-III source.

In Solid-source MBE growth, the source materials in high purity crucibles in cells, known as Knudsen cells or effusion cells are heated to evaporate

the growth materials. This forms beams of homoatomic molecules, such as Ga, As_2, As_4, and Si. The beam of these molecules are directed towards the substrate that can be heated and rotated for the uniformity of deposition. The flux rate of the molecular beam is controlled by adjusting the effusion cell temperature, and determined by an ion gauge. The morphology of the growing surface depends on the substrate temperature, the surface material, the crystallographic orientation, the flux rates [5]. A schematic diagram of an MBE growth chamber is shown in Figure 2.1.
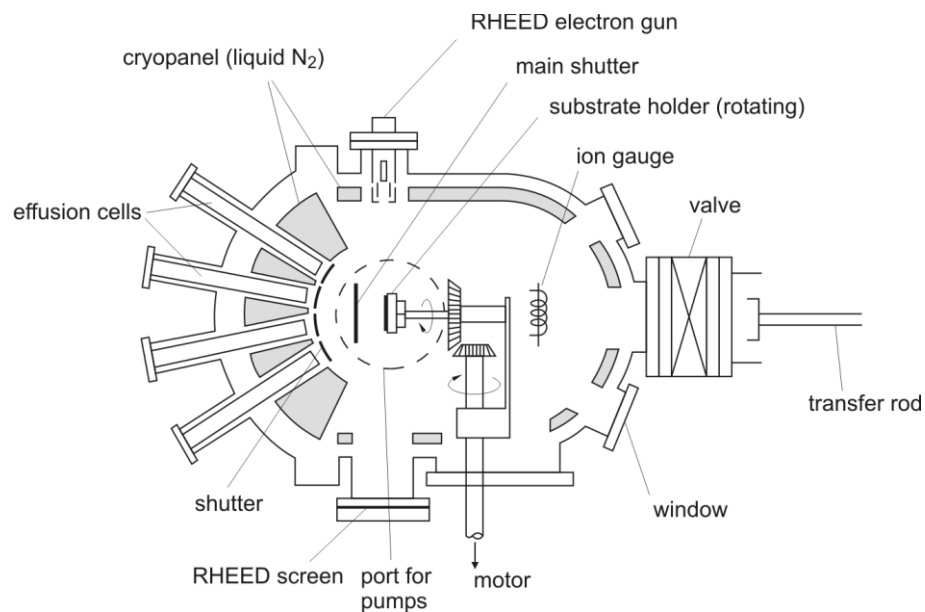
Figure 2.1 Schematic diagram of an MBE growth chamber (taken from [6]).

In order to reduce the background pressure of contaminants, the growth chamber of an MBE is kept under ultra-high vacuum (~ 10^{-11} Torr). The ultra-high vacuum condition is maintained by the liquid nitrogen-cooled

cryopanels. The effusion cells have a mechanical shutter with a short actuation time (< 0.1 s) that enables an abrupt change of composition, and deposition of less than a monolayer of material. During the growth, reflection high energy electron diffraction (RHEED) is used to monitor the change of the growing surface.

2.2.1 Molecular beam epitaxy growth mechanism

It has been shown that the growth of group-III species involves initial chemisorption onto the growing surface before they migrate to suitable lattice sites to be incorporated [7]. On the other hand, group-V species have been shown to be physisorbed to the growing surface and incorporated by bonding to a cation [7]. This is because group-III elements have unity sticking coefficients to the substrate surfaces, whereas group-V elements do not stick to the surface in the absence of group-III atoms at typical growth temperatures [2]. This means that excess group-V atoms are desorbed from the surface and hence, the growth rate of III-V compounds is solely governed by the flux of the group-III atoms.

When a lattice-mismatched heteroepitaxial structure is grown in 2D layer-by-layer growth mode, the epilayer is forced to fit the lattice constant of the growing surface. This leads to a misfit strain in a layer known as the wetting layer. As the thickness of the wetting layer increases, eventually the

accumulated strain is relaxed by forming three-dimensional islands. The transition occurs when the coverage of the growth material exceeds the critical coverage that depends on the lattice mismatch, and growth conditions, such as growth temperature and growth rate [8]. The growth mode in which three-dimensional islands are formed is known as Stranski-Krastanow (SK) growth [9]. SK growth is the mechanism by which self-assembled quantum dots (QDs) are grown. Another growth mode that is based on lattice-matched system is Volmer-Weber (VW) morphology. VW growth leaves some parts of the substrate exposed and forms no wetting layer.

2.2.2   Self-assembled quantum dots

QDs are nano-sized crystals of semiconductor material that are confined in all three dimensions. The growth of QDs can be achieved when self-assembled three dimensional islands are grown by Stranski-Krastanow growth mode. The requirement for achieving the three-dimensional quantum confinement is that the mean free path and the de Broglie wavelength of carriers need to be greater than the critical size of nanostructures (i.e. quantum dots) [10]. In III-V QDs mismatched heteroepitaxial systems, such as InAs/GaAs [11], [12], InAsSb/GaAs[13], InAs/GaAsSb [14], [15], InAs/InGaP [16], and InP/GaAs [17], the shapes of the QDs have been observed to be elongated truncated pyramids with

typical base diameters and heights in the order of a few tens of nanometres and few nanometres, respectively. InAs QDs on GaAs is the most studied QD system to date due to its small lattice-mismatch (~ 7 %). The critical thickness for surface elastic relaxation of InAs islands on GaAs is 1.50 ML [18]. Usually, a few seconds of growth interruption is implemented after the formation of quantum dots in order to improves the size uniformity of QDs [19]. Another factor that can affect the crystal quality of InAs QDs is the growth rate and As pressure in the growth chamber. It has been shown that a low growth rate and a high arsenic pressure lead to the formation of high quality InAs QDs.

When multiple layers of QDs are grown on top of each other, the lattice distortion and the interdiffusion of species can cause changes in the morphology and the composition of QDs. Therefore, QD layers are usually separated by a spacer layer to ensure that the strain field induced by the QDs in a layer does not affect the morphology and the composition of dots in upper layers.

One of the advantages of using QDs for optoelectronic applications is that the bandgap of the material can be precisely tuned by controlling the size of QDs. In addition to this, QD devices are less susceptible to edge or surface recombination as QDs structures suppress the lateral migration of

carriers [20]. Also, their insensitivity to temperature changes has proved promising for laser and concentrator solar cells [21]. Furthermore, it has been shown that QD solar cells have higher radiation tolerance compared with bulk solar cells, which can be useful for space applications [22].

2.3   Device processing

Following the epitaxial growth using the MBE, solar cell structures need to undergo the device fabrication stage. During the device fabrication, metal contacts are deposited on the solar cell structure to allow the extraction of current and voltage. Five major steps involved in the standard semiconductor lithography method for the fabrication of GaAs solar cells are cleaning, photolithography, wet etching, metallisation and thermal annealing.

However, in this project, photolithography is replaced with the metal mask method. In the metal mask method, a thin metal mask is used to define patterns for metallisation as opposed to an optical mask for the photolithography technique, and metal contacts are deposited directly through the metal mask and on the wafer sample. Although the dimensions of the front contact grid patterns occupy a larger area of wafer, the fabrication of solar cells can be simplified in this way. The steps that were used for solar cell processing with this method are listed below.

2.3.1   Sample cleaving

Firstly, the wafers are cleft into a suitable size for the metal mask. With the metal mask that was used in this project, a wafer sample of 12 mm × 12 mm can accommodate 4 solar cells. The mask grid pattern and the corresponding dimensions are shown in Figure 2.2.

Ⓐ	0.04 cm
Ⓑ	0.02 cm
Ⓒ	0.03 cm
Width	0.45 cm
Length	0.45 cm
Metal Contact Area	0.11 cm²
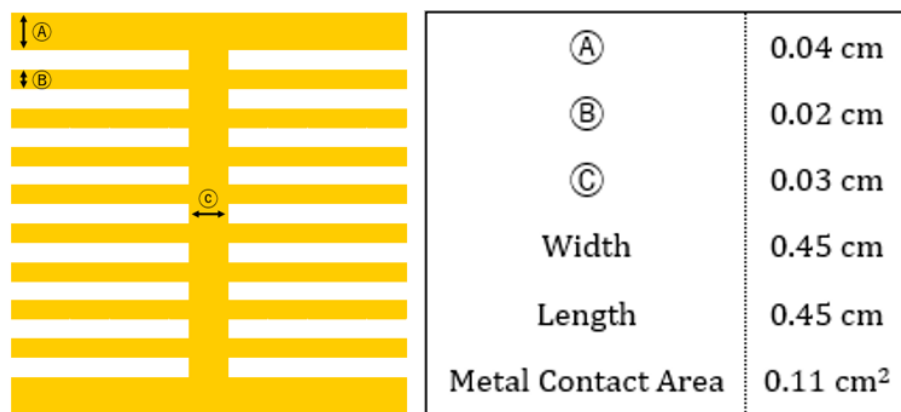
Figure 2.2 Metal mask grid pattern (left) and the corresponding dimensions (right).

2.3.2 Cleaning and oxide removal

To fabricate devices with a high quality and reproducibility, the fabrication process must be free of contaminants. The cleaning process ensures that unwanted materials are removed before subsequent processes are carried out. Organic solvents, such as acetone and isopropyl alcohol (IPA), are used to remove oils and organic materials. The cleft samples wafers are ultrasonicated in acetone and then IPA for 5 mins each time for the cleaning. The cleaning process is followed by the surface oxide removal. The surface oxide is etched in a solution of NH_3:de-ionised (DI) water (1:19) for 30 s. Samples are then rinsed in (DI) water and blown dry with N_2.

2.3.3 Metallisation

Thermal evaporators are used to deposit the metal contacts on solar cell samples to create ohmic contacts. An ohmic contact has a thin Schottky barrier that allows conduction across the metal-semiconductor junction by tunneling. For this, the surface layer of the semiconductor material need to be highly doped. For an n-type metal contact, a system such as Au-Ge, Au-Ge-Ni and InGe-Au are typically used, whereas for a p-type metal contact, Zn/Au and AuBe-Au have been shown to produce ohmic contacts with a contact resistance of 10^{-5} Ωcm^2. For the test solar cell samples, Zn-Au alloy (95 % Au, 5 % Zn, 200 nm) is used for the p-type contact and Ni/Ge-Au alloy (88 % Au, 12 % Ge)/Ni/Au (10 nm/100 nm/30 nm/200 nm) is used for the n-contact. A multi-source evaporator system is used with a film thickness crystal monitor ensuring the correct layer thicknesses.

2.3.4 Thermal annealing

The thermal annealing is the final step followed by the metallisation. For the annealing, a rapid thermal processing (RTP) equipment is used to heat the sample at a fixed temperature for duration of time. This process aids the formation of an ohmic contact. The solar cell samples are annealed in a RTP equipment at 400 ºC for 30 s seconds in foaming gas (95% N_2, 5% H_2) or N_2 atmosphere.

2.4   References

[1]   H. Cöelfen and M. Antonietti, *Mesocrystals and Nonclassical Crystallization*. John Wiley & Sons, 2008.

[2]   A. Y. Cho and J. R. Arthur, 'Molecular beam epitaxy', *Prog. Solid State Chem.*, vol. 10, pp. 157–191, Jan. 1975.

[3]   A. Y. Cho, 'How molecular beam epitaxy (MBE) began and its projection into the future', *J. Cryst. Growth*, vol. 201–202, pp. 1–7, May 1999.

[4]   J. R. Arthur, 'Molecular beam epitaxy', *Surf. Sci.*, vol. 500, no. 1–3, pp. 189–217, Mar. 2002.

[5]   K. Barnham and D. Vvedensky, *Low-Dimensional Semiconductor Structures: Fundamentals and Device Applications*. Cambridge University Press, 2008.

[6]   H. Ibach and H. Lüth, *Solid-State Physics: An Introduction to Principles of Materials Science*. Springer Science & Business Media, 2009.

[7]   J. R. A. Jr, 'Interaction of Ga and As2 Molecular Beams with GaAs Surfaces', *J. Appl. Phys.*, vol. 39, no. 8, pp. 4032–4034, Jul. 1968.

[8]   C. Heyn, 'Critical coverage for strain-induced formation of InAs quantum dots', *Phys. Rev. B*, vol. 64, no. 16, p. 165306, Oct. 2001.

[9]   I. N. Stranski and L. von Krastanow, 'Sitzungsber. Akad. Wiss. Wien, Math', *Naturwiss Kl Abt B*, vol. 2, no. 146, p. 797, 1937.

[10] S. Franchi, G. Trevisi, L. Seravalli, and P. Frigeri, 'Quantum dot nanostructures and molecular beam epitaxy', *Prog. Cryst. Growth Charact. Mater.*, vol. 47, no. 2–3, pp. 166–195, 2003.

[11] H. Y. Liu, B. Xu, Y. H. Chen, D. Ding, and Z. G. Wang, 'Effects of seed layer on the realization of larger self-assembled coherent InAs/GaAs quantum dots', *J. Appl. Phys.*, vol. 88, no. 9, pp. 5433–5436, Nov. 2000.

[12] P. Lam *et al.*, 'Voltage recovery in charged InAs/GaAs quantum dot solar cells', *Nano Energy*, vol. 6, pp. 159–166, May 2014.

[13] M. Kudo, T. Nakaoka, S. Iwamoto, and Y. Arakawa, 'InAsSb Quantum Dots Grown on GaAs Substrates by Molecular Beam Epitaxy', *Jpn. J. Appl. Phys.*, vol. 44, no. 1, pp. L45–L47, Jan. 2005.

[14] S. P. Bremner *et al.*, 'Growth of InAs quantum dots on GaAsSb for the realization of a quantum dot solar cell', in *33rd IEEE Photovoltaic Specialists Conference, 2008. PVSC '08*, 2008, pp. 1–6.

[15] S. Hatch *et al.*, 'InAs/GaAsSb quantum dot solar cells', *Opt. Express*, vol. 22, no. S3, pp. A679–A685, May 2014.

[16] P. Lam *et al.*, 'InAs/InGaP quantum dot solar cells with an AlGaAs interlayer', *Sol. Energy Mater. Sol. Cells*, vol. 144, pp. 96–101, Jan. 2016.

[17] M. P. F. de Godoy *et al.*, 'Structural and optical properties of InP quantum dots grown on GaAs(001)', *J. Appl. Phys.*, vol. 101, no. 7, p. 073508, Apr. 2007.

[18] D. Leonard, K. Pond, and P. M. Petroff, 'Critical layer thickness for self-assembled InAs islands on GaAs', *Phys. Rev. B*, vol. 50, no. 16, pp. 11687–11692, Oct. 1994.

[19] S. Kiravittaya, Y. Nakamura, and O. G. Schmidt, 'Photoluminescence linewidth narrowing of InAs/GaAs self-assembled quantum dots', *Phys. E Low-Dimens. Syst. Nanostructures*, vol. 13, no. 2–4, pp. 224–228, Mar. 2002.

[20] D. P. Popescu, P. G. Eliseev, A. Stintz, and K. J. Malloy, 'Carrier migration in structures with InAs quantum dots', *J. Appl. Phys.*, vol. 94, no. 4, pp. 2454–2458, Aug. 2003.

[21] M. Sugawara and M. Usami, 'Quantum dot devices: Handling the heat', *Nat. Photonics*, vol. 3, no. 1, pp. 30–31, Jan. 2009.

[22] C. D. Cress, S. M. Hubbard, B. J. Landi, R. P. Raffaelle, and D. M. Wilt, 'Quantum dot solar cell tolerance to alpha-particle irradiation', *Appl. Phys. Lett.*, vol. 91, no. 18, p. 183108, Oct. 2007.

Chapter 3
Si-doped InAs/GaAs quantum dot solar cells with AlAs cap layers

One of the requirements for strong sub-bandgap photon absorption in the quantum dot intermediate band solar cell is the partial filling of the intermediate band. Studies have shown that the partial filling of the intermediate band can be achieved by introducing Si doping to the quantum dots. However, the existence of too many Si dopants has been shown to cause the formation of point defects, and hence the reduction of photocurrent. In this chapter, the use of direct Si doping in InAs/GaAs QDSCs with AlAs cap layers (CLs) for the saturation of strain-induced dislocations and QD state filling is demonstrated. Previously, Tutu et al. reported that the deposition of AlAs CLs on InAs QDs could suppress the formation of the WL [1]. As a result of the WL removal, the effective bandgap of the QDSC was increased, which in turn led to the increase in

the thermal activation energy and the VOC. In this work, in addition to the enhancement of the VOC by applying AlAs CLs, a further increase in the VOC by ~ 44 mV is observed by passivating the defect states with moderate Si doping (6 e/dot). Also, the QD state filling, which is essential for strong two-photon absorption, is observed with significantly lower Si doping densities when compared with that reported by Lam et al. [2].

3.1   Experimental work

3.1.1   Growth details

The InAs/GaAs QDSC samples with AlAs CLs were grown by a solid-source molecular beam epitaxy (MBE) on n$^+$ GaAs (100) substrates. As shown in

Figure 3.1, all SCs were grown with the same p-i-n structure that consists of a 200 nm GaAs buffer layer with Si doping density of 1×10^{18} cm^{-3}, 30 nm Al$_{0.35}$Ga$_{0.65}$As back surface field (BSF) with Si doping density of 1×10^{18} cm^{-3}, 1000 nm GaAs base with Si doping density of 1×10^{17} cm^{-3}, 250 nm GaAs emitter with Be doping density of 2×10^{18} cm^{-3}, 30 nm Al$_{0.75}$Ga$_{0.25}$As window layer with Be doping density of 2×10^{18} cm^{-3}, and 50 nm GaAs contact layer with Be doping density of 1×10^{19} cm^{-3}. The intrinsic region of the SCs consists of 20 stacks of 2.1 monolayer (ML) InAs QDs with 2 ML AlAs CLs separated by a 20 nm GaAs spacer. The QDs were grown by the

Stranski-Krastanov mode at substrate temperature of ~ 500 °C. High-growth-temperature GaAs spacer layers were applied during the growth of QDs to suppress the formation of dislocations [3]–[5]. The QDSCs were Si-doped with four different doping densities of 0, 6, 12, and 18 e/dot. It should be noted that the effective QD doping density depends on the drift-diffusion of free carriers in the bulk and the net capture rate in the QDs, which can lead to fluctuation across the QD layers and different QD doping densities from the nominal values.

50 nm p$^+$ GaAs	[Be: 1×10^{19} cm^{-3}]
30 nm p Al$_{0.75}$Ga$_{0.25}$As window	[Be: 2×10^{18} cm^{-3}]
250 nm p GaAs emitter	[Be: 2×10^{18} cm^{-3}]
15 nm i GaAs	
5 nm i GaAs	2 ML AlAs cap
▲▲▲▲▲▲▲▲▲▲▲▲▲▲▲▲▲▲▲▲▲▲▲▲▲▲▲▲	
20 nm i GaAs	2.3 ML InAs QDs
1000 nm n$^-$ GaAs base	[Si: 1×10^{17} cm^{-3}]
30 nm n$^+$ Al$_{0.35}$Ga$_{0.65}$As BSF	[Si: 1×10^{18} cm^{-3}]
200 nm n$^+$ GaAs buffer	[Si: 1×10^{18} cm^{-3}]
n$^+$ GaAs (001) substrate	

× 20
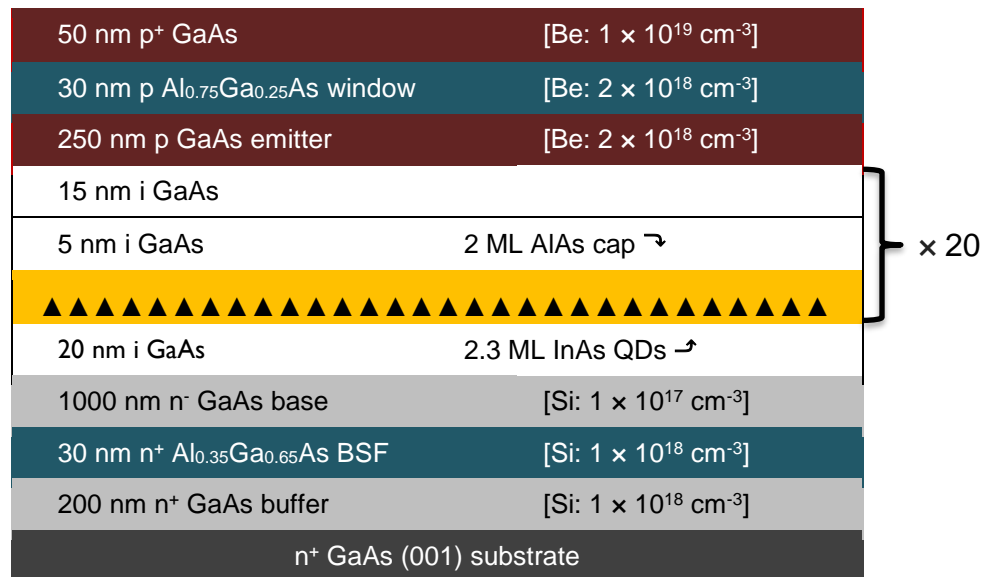
Figure 3.1. Structure of the Si-doped (0, 6, 12, 18 e/dot) InAs/GaAs QDSCs with AlAs CLs.

3.1.2   Device processing

For the sample cleaning, the SCs were ultrasonicated first in acetone and then in isopropanol for 10 mins each. The surface oxide removal was performed by immersing the SCs in dilute ammonia solution (1:19) for 30 s. A Au-Zn alloy (95 % Au, 5 % Zn) was thermally evaporated to form a (~ 200 nm thick) grid-pattern p-type electrode using a metal shadow mask. For the n-type electrode, 10 nm Ni, 100 nm Au-Ge (88 % Au, 12 % Ge), 30 nm Ni, and 200 nm Au were thermally evaporated onto the entire back surface, and thermally annealed at 400 °C for 60 s. No anti-reflective coating or surface passivation was applied to these SCs.

3.1.3 Device characterization

A Veeco Nanoscope V atomic force microscope (AFM) was used to characterise the morphology of an uncapped QD layer. Temperature-dependent and power-dependent photoluminescence (PL) measurements were performed using 532 nm excitation from a diode-pumped solid-state laser. The sample temperature between 10 K and 300 K was controlled using a He-cooled cryostat during the PL measurements. The transient PL measurements were performed with 2 ps pulses at excitation of 750 nm from a mode-locked Ti: sapphire laser that produces an optical pulse train at 76 MHz. Also, a Hamamatsu Synchroscan streak camera C5680 with an infrared enhanced S1 cathode was used for the transient PL signal detection. Current density vs voltage (J-V) characteristics were obtained by using an LOT calibrated solar simulator with a xenon lamp under one-sun air mass (AM) 1.5 G illumination at room temperature. A 4-point probe station was used to connect devices to a Keithly 2400 sourcemeter that outputs the data to ReRa Tracer 3 software. Photocurrent measurements were performed with a halogen lamp chopped to a frequency of 188 Hz through a Newport monochromator. The monochromatic beam was calibrated with a silicon photo-diode and the data was analysed with ReRa Photor QE 3.1 software to obtain the external quantum efficiency (EQE) at room temperature.

3.2 Results and discussion

3.2.1 Structural characterisation

AFM was used to analyse the morphology of InAs QDs on GaAs, as shown in Figure 3.2. The average diameter of the QDs was measured to be ~ 30 nm, with an average height of ~ 5 nm. No large defective clusters were observed, which indicates a high structural quality [6]. The dot density was estimated to be ~ 2.3 × 10^{10} cm^{-2}.
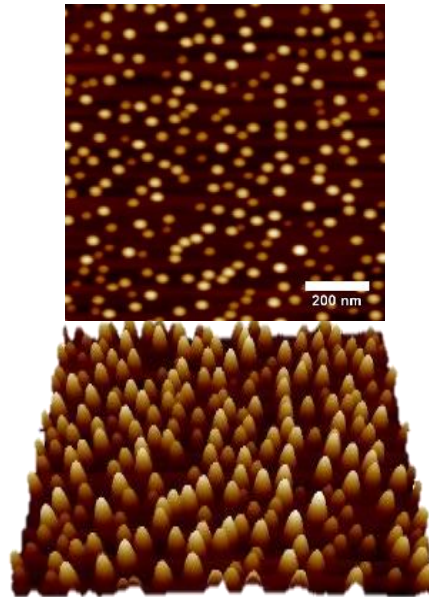
Figure 3.2. AFM images of InAs QDs grown on GaAs in 2D (top) and 3D (bottom).

3.2.2   Optical characterisation

The optical properties of the Si-doped InAs/GaAs QDs with AlAs CLs were compared. Figure 3.3 (a) shows the normalised PL spectra for the QDSCs at 10 K. Two peaks are observed from the PL spectrum of the undoped QDSC (0 e/dot) at ~ 830 nm and ~ 1050 nm. The peak at the lower wavelength originates from GaAs, whereas the peak at the higher wavelength corresponds to the ground state of the InAs QDs. The spectra display additional QD emission peaks (950 – 1100 nm) for the samples with higher Si doping. This can be explained by the emissions related to excited state transitions observed at lower wavelengths alongside the ground state emission [7]. Although the higher-energy emission peaks can originate from the phonon bottleneck, segregated inhomogeneous broadening, and state filling, it is possible to distinguish them by performing a power-dependent PL study. When the phonon bottleneck effect gives rise to higher-energy emission peaks, the excited state interband transitions are observable even under low excitation conditions as the relaxation dynamics of intersublevel and interband are comparable [8]. In the case of segregated inhomogeneous broadening, the emission peaks keep the same relative magnitude over several orders of magnitude of excitation intensity [7]. In contrast, the excited state PL peaks become less prominent with decreasing excitation power in the case of state filling [9]. Figure 3.3 (b) shows the normalised power-dependent PL spectra for the QDSC with Si

doping density of 18 e/dot. It can be seen that with decreasing laser excitation power, the relative magnitudes of the peaks observed between 950 nm and 1025 nm decrease, when compared with that of the peak observed at ~ 1080 nm. However, at higher laser excitation powers, two higher-energy peaks become more prominent. The inference to be drawn from this is that these emission peaks are caused by the state filling effect; the lowest-energy peak being the ground state, and the higher-energy peaks being the excited states. The trend that the excited state emissions become more prominent with higher Si doping density, from Figure 3.3 (a), indicates that the doping results in state filling effect. In the study performed by Lam et al. [2], even though the dopants were directly supplied to the QDs, some dopants remained in the WL, and were used to form a potential barrier between the WL and QDs. In this work, in contrast, the formation of WL was prevented by applying AlAs CLs on QDs during the MBE growth [1]. In this manner, most electrons from Si doping can be incorporated in the QDs and be used for state filling.
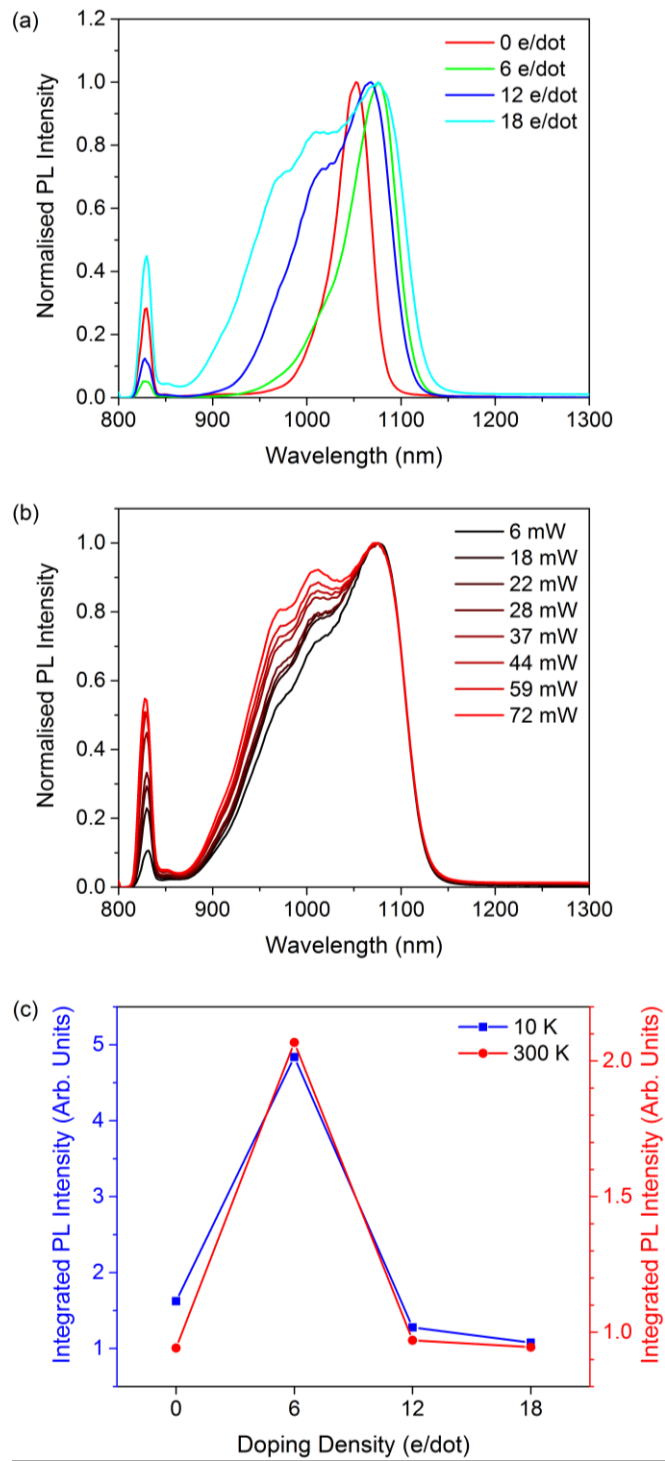
Figure 3.3. (a) Normalised PL spectra of Si-doped (0, 6, 12, 18 e/dot) QDSCs with AlAs cap layer measured at 10 K (P_{ex} = 37 mW). (b) Normalised power-dependent PL stectra for 18 e/dot QDSC at 10 K. (c) Integrated PL intensity vs. Si doping density at 10 K (I_{ex} = 386 W/cm^2, $λ_{ex}$ = 532 nm) and 300 K (I_{ex} = 459 W/cm^2, $λ_{ex}$ = 635 nm).

Figure 3.3 (c) shows the integrated PL intensity as a function of Si doping density, at 10 K and 300 K. It can be seen that the QDSC with doping density of 6 e/dot exhibits the strongest PL peak intensity. The enhancement of the PL intensity can be attributed to the passivation of the defect states by Si doping, which leads to suppression of the non-radiative process [10], [11]. However, Figure 3.3 (c) shows that any further increase in the Si doping level results in a dramatic decrease in the PL intensity. This can be due the presence of too many Si atoms, which can cause destruction of the crystal lattice of the InAs QDs and formation of non-radiative recombination centres [12].
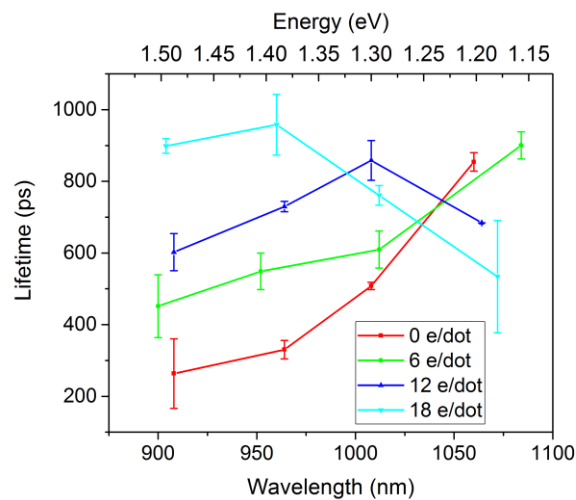
Figure 3.4. Carrier lifetime versus wavelength obtained from the transient photoluminescence spectra of the Si-doped QDSCs with AlAs cap layers at 10 K (λ_{ex} = 750 nm)

In order to provide further evidence of the QD state filling and the passivation of the defect states achieved by Si doping, a time-resolved PL

study was performed for the QDCSs at 10 K. Figure 3.4 shows that the carrier lifetime in the region of 875 - 925 nm increases with increasing Si doping density. This can be linked to the state filling effect observed from the steady-state PL measurements. The appearance of the higher-energy QD emission peaks with higher Si doping densities in Figure 3.3 (a) indicates that the additional electrons supplied by the Si dopants are used to fill the QD states. In other words, with more QD states filled with electrons, less available decay channels will exist for the carriers, which in turn results in longer lifetimes. In contrast, the carrier lifetime of the QD ground state (1050 – 1100 nm) in Figure 3.4 shows that increasing Si doping density leads to an initial increase with moderate doping density (6 e/dot), followed by a significant drop in the carrier lifetime with higher doping densities (12, 18 e/dot). This trend is similar to that observed in the integrated PL intensity measurements, shown in Figure 3.3 (c). Therefore, it can be inferred the initial increase in the carrier lifetime with doping density of 6 e/dot originates from the passivated defect states. However, once all defect states are filled, further addition of Si atoms leads to formation of non-radiative recombination centres, which decreases the carrier lifetime.

3.2.3   Solar cell performance characterisation

The EQE spectra of the Si-doped QDSCs with AlAs CLs are presented in Figure 3.5. For all doped samples, there is a drop in EQE at ~ 870 nm which corresponds to the bandgap of GaAs. At the higher wavelengths, flat spectral responses without a WL peak (~ 915 nm) are observed. The sub-bandgap EQE spectra shown in the inset of Figure 3.5 depicts decreasing EQE contribution from the QDs with increasing doping density. This is mainly attributed to the extra electrons introduced by Si doping filling the CB of the QDs, which decreases the probability of the VB to CB transition of electrons in the QDs. As a result, the absorption from the QDs is weakened [12]. Another possible cause for the reduced EQE can be the suppression of the thermal escape of the photo-excited carriers due to the formation of a potential barrier at QD/WL interface by Si doping, as reported by Lam et al. [2]. However, with the AlAs capping layer, it is expected that the formation of such a potential barrier be minimised. It can also be noted from Figure 3.5 that the supra-bandgap (400 – 870 nm) absorption of all QDSCs with Si doping is significantly reduced when compared with that of the undoped QDSC. This can be attributed to the decrease in depletion region after Si doping, which reduces the effective absorption area. At the same time, the reduction in the supra-bandgap EQE could also be linked to the introduction of Si dopants. The Si dopants can substitute the Ga and As

sites or exist as interstitials [13], [14]. This leads to the formation of point

defects, and hence reduction in the EQE response.
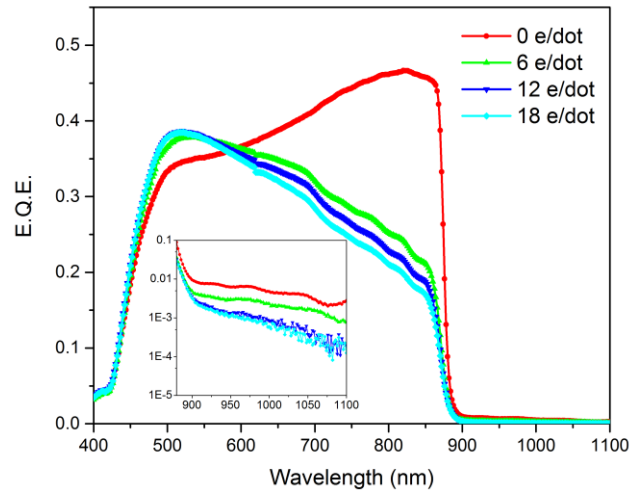
Figure 3.5. External quantum efficiency spectra of Si-doped (0, 6, 12, 18 e/dot) QDSCs with AlAs cap layers.
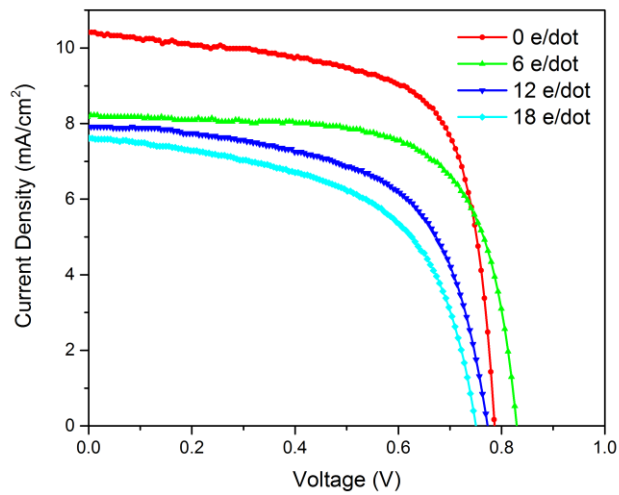
Figure 3.6. Current density versus voltage behaviour of Si-doped QDSCs with AlAs cap layers under one-sun (AM 1.5G) illumination

Table 3.1 Current density, open-circuit voltage, fill factor, and efficiency measured from Si-doped QDSCs with AlAs cap layers

Device	J_{SC} (mA/cm^2)	V_{OC} (V)	FF (%)	η (%)
0 e/dot	10.41	785.76	68.49	5.60
6 e/dot	8.19	829.34	69.04	4.69
12 e/dot	7.91	772.40	60.69	3.71
18 e/dot	7.61	749.82	56.98	3.25

The current density-voltage characteristics of the QDSCs in Figure 3.6 and Table 3.1 show a clear dependence on the Si-doping density. Firstly, all Si-doped samples display a significant drop in the current density when compared with the undoped sample. This can be related to the reduction in the EQE contribution from the supra-bandgap region observed in Figure 3.5. In other words, the decrease in the depletion region width caused by the introduction of Si dopants results in a reduction in the effective area for absorption, and hence a decrease in the current density. Secondly, a further gradual decrease in the current density with increasing doping is observed amongst the doped QDSCs. This is likely to be due to the point defects formed by Si dopants substituting Ga and As or existing as interstitials [13], [14]. The defect states induced by Si doping increase Shockley-Read-Hall recombination, decrease the minority carrier lifetime,

and consequently lower the current density. Although Si doping has a negative impact in the current density, an enhancement of the open-circuit voltage is observed with moderate doping density. The open-circuit voltage increases from 0.783 V for the 0 e/dot QDSC to 0.826 V for the 6 e/dot QDSC. This agrees well with the trend observed in the PL intensity measurements shown in Figure 3.3 (c). Both the PL intensity and the open-circuit voltage reach their maxima at 6 e/dot, which is likely to be due to the moderate Si doping passivating the defect states. However, further increase in the Si doping leads to a gradual decrease in the open-circuit voltage, which also corresponds well with the decreasing trend of the PL intensity that originates from the formation of non-radiative recombination centres due to the excessive amount of Si.

3.3   Conclusion

In conclusion, an improvement in the V_{OC} (~ 44 mV) has been achieved by introducing direct Si doping to QDs with AlAs CLs. The increase in the V_{OC} is attributed to the passivation of the defect states with moderate Si doping (6 e/dot), alongside the reduced CB-IB thermal coupling with AlAs CLs. Also, with the AlAs CLs, the QD state filling effect is observed with low Si doping densities. The factors that contributed to the decrease in the supra-bandgap EQE and the photocurrent after Si doping, such as the decrease in depletion region and the formation of point defects, should be taken into account when designing future Si-doped QDSCs. Nonetheless, the results presented in this chapter hold some promise for overcoming some of the main challenges in implementing QD-IBSCs with the efficiencies close to that of the theoretical model of the IBSC.

3.4   References

[1]   F. K. Tutu *et al.*, 'InAs/GaAs quantum dot solar cell with an AlAs cap layer', *Appl. Phys. Lett.*, vol. 102, no. 16, p. 163907, Apr. 2013.

[2]   P. Lam *et al.*, 'Voltage recovery in charged InAs/GaAs quantum dot solar cells', *Nano Energy*, vol. 6, pp. 159–166, May 2014.

[3]   F. K. Tutu *et al.*, 'Improved performance of multilayer InAs/GaAs quantum-dot solar cells using a high-growth-temperature GaAs spacer layer', *J. Appl. Phys.*, vol. 111, no. 4, p. 046101, Feb. 2012.

[4]   H. Y. Liu *et al.*, 'Improved performance of 1.3µm multilayer InAs quantum-dot lasers using a high-growth-temperature GaAs spacer layer', *Appl. Phys. Lett.*, vol. 85, no. 5, pp. 704–706, Aug. 2004.

[5]   H. Y. Liu *et al.*, 'p-doped 1.3µmInAs/GaAs quantum-dot laser with a low threshold current density and high differential efficiency', *Appl. Phys. Lett.*, vol. 89, no. 7, p. 073113, Aug. 2006.

[6]   H. Y. Liu *et al.*, 'Influences of the spacer layer growth temperature on multilayer InAs/GaAs quantum dot structures', *J. Appl. Phys.*, vol. 96, no. 4, pp. 1988–1992, Aug. 2004.

[7]   M. V. Marquezini, M. J. S. P. Brasil, J. A. Brum, P. Poole, S. Charbonneau, and M. C. Tamargo, 'Study of temperature-dependent exciton dynamics in a single quantum well with self-assembled islands', *Surf. Sci.*, vol. 361–362, pp. 810–813, Jul. 1996.

[8]   K. Brunner *et al.*, 'Photoluminescence from a single GaAs/AlGaAs quantum dot', *Phys. Rev. Lett.*, vol. 69, no. 22, pp. 3216–3219, Nov. 1992.

[9]   Z. M. Wang, *Self-Assembled Quantum Dots*. Springer Science & Business Media, 2007.

[10] K. A. Sablon, J. W. Little, V. Mitin, A. Sergeev, N. Vagidov, and K. Reinhardt, 'Strong Enhancement of Solar Cell Efficiency Due to Quantum Dots with Built-In Charge', *Nano Lett.*, vol. 11, no. 6, pp. 2311–2317, 2011.

[11] T. Inoue, S. Kido, K. Sasayama, T. Kita, and O. Wada, 'Impurity doping in self-assembled InAs/GaAs quantum dots by selection of growth steps', *J. Appl. Phys.*, vol. 108, no. 6, p. 063524, Sep. 2010.

[12] X. Yang *et al.*, 'Improved efficiency of InAs/GaAs quantum dots solar cells by Si-doping', *Sol. Energy Mater. Sol. Cells*, vol. 113, pp. 144–147, Jun. 2013.

[13] D. T. J. Hurle, 'A comprehensive thermodynamic analysis of native point defect and dopant solubilities in gallium arsenide', *J. Appl. Phys.*, vol. 85, no. 10, pp. 6957–7022, May 1999.

[14] D. T. J. Hurle, 'A thermodynamic analysis of native point defect and dopant solubilities in zinc-blende III–V semiconductors', *J. Appl. Phys.*, vol. 107, no. 12, p. 121301, Jun. 2010.

Chapter 4
Type-II InAs/GaAsSb quantum dot solar cells with GaAs interlayers

One of the primary challenges facing quantum dot-based intermediate band solar cells is the short lifetime of charge carriers. In a solar cell with a type-I band alignment, electrons and holes are confined in the same spatial region. Typically, a type-I band alignment formed by InAs/GaAs QD SCs allows efficient radiative recombination, resulting in short carrier lifetimes (~ 1 ns). However, in a solar cell with type-II band alignment, electrons and holes are spatially separated, which can prolong the carrier lifetime [1]–[3]. GaAsSb enables the formation of a type-II band alignment for InAs/GaAsSb QD system. Valence band offset (VBO) between the InAs QDs and GaAs$_{1-x}$Sb$_x$ QW depends on the Sb composition; the crossover between type-I and type-II band alignment is reported to occur when $x = 0.12$ [4]–[6].

We previously demonstrated enhanced type-II characteristics in the InAs-QD/GaAs$_{0.83}$Sb$_{0.17}$-QW hybrid SC when a GaAs interlayer was inserted between the InAs QDs and GaAsSb QW [7]. A 23% improvement in power conversion efficiency was observed compared with the structure without the GaAs interlayer. This behaviour was attributed to a reduction in VB confinement in the GaAsSb QW, which lowered the potential barrier for hole transport across the active region. To further examine this phenomenon, hybrid InAs-QD/GaAs$_{1-x}$Sb$_x$-QW SCs with a GaAs interlayer with four Sb compositions (x = 0, 0.08, 0.14, and 0.17) are studied. Laser power-dependent, temperature-dependent, and time-resolved photoluminescence (PL) measurements are used to investigate the radiative emission pathways and identify the presence of type-II band alignment. Current density vs. voltage (J-V) and external quantum efficiency (EQE) measurements are used to characterise the SC performance and demonstrate the benefit of introducing a GaAs interlayer to the type-II InAs-QD/GaAsSb-QW SCs.

4.1 Experimental work

4.1.1 Growth details

Four hybrid InAs-QD/GaAsSb-QW SC samples were grown by a solid-source molecular beam epitaxy (MBE) on n^+-GaAs (100) substrates. As shown in Figure 3.1, all SCs are grown with the same p-i-n structure that consists of a 200 nm GaAs buffer layer with Si doping density of 2×10^{18} cm^{-3}, 50 nm Al$_{0.35}$Ga$_{0.65}$As back surface field layer with Si doping density of 2×10^{18} cm^{-3}, 1000 nm GaAs base with Si doping density of 2×10^{17} cm^{-3}, 100 nm GaAs emitter with Be doping density of 1×10^{18} cm^{-3}, 100 nm GaAs emitter with Be doping density of 5×10^{18} cm^{-3}, 30 nm Al$_{0.79}$Ga$_{0.21}$As window layer with Be doping density of 5×10^{18} cm^{-3}, and 20 nm GaAs contact layer with Be doping density of 1×10^{19} cm^{-3}. The intrinsic region of the SCs consists of 20 stacks of hybrid InAs-QDs/GaAs$_{1-x}$Sb$_x$ QWs separated by a 45 nm GaAs spacer. High-growth-temperature GaAs spacer layers are applied during the growth of QDs to suppress the formation of dislocations [8]–[10]. To form hybrid InAs-QD/GaAsSb-QW structure, a 2 nm GaAs interlayer is inserted between 2.1-MLs InAs QDs and 5-nm GaAs$_{1-x}$Sb$_x$-QW. The QDs are grown by the Stranski-Krastanov mode at substrate temperature of ~ 485 °C measured by a pyrometer.

| 20 nm p$^+$ GaAs |
| 30 nm p Al$_{0.75}$Ga$_{0.25}$As Window |
| 100 nm p GaAs Emitter |
| 100 nm p$^-$ GaAs Emitter |
| 45 nm i GaAs Spacer |
| 2 nm i GaAs Interlayer |
| 5 nm i GaAs$_{1-x}$Sb$_x$ QW |
| 45 nm i GaAs Spacer |
| 1000 nm n$^-$ GaAs Base |
| 50 nm n Al$_{0.35}$Ga$_{0.65}$As BSF |
| 200 nm n GaAs Buffer |
| n$^+$ GaAs (001) Substrate |

× 20
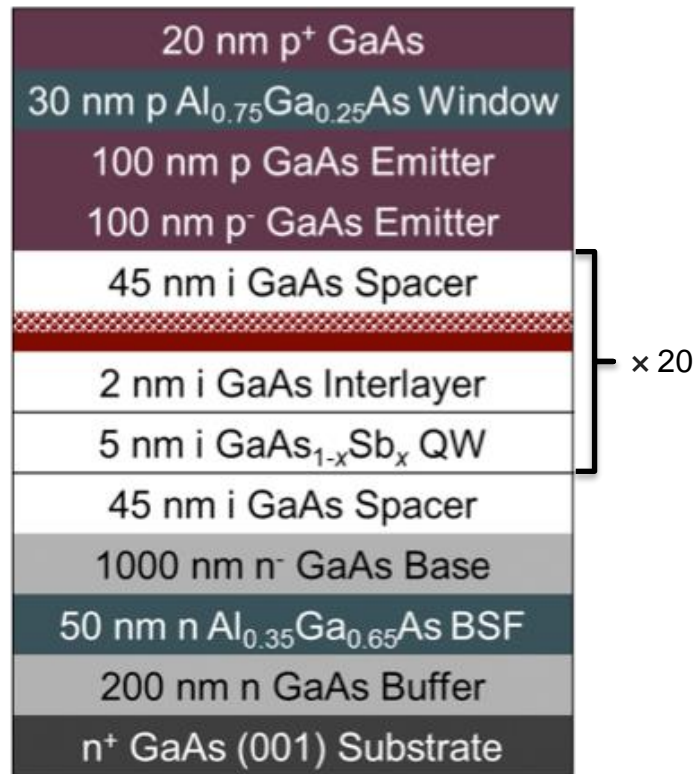
Figure 4.1. Structure of the hybrid InAs-QD/GaAs$_{1-x}$Sb$_x$-QW SCs (x = 0, 0.08, 0.14, and 0.17).

4.1.2 Device processing

For device fabrication, a Au-Zn (5%) alloy is thermally evaporated to form a (~220 nm thick) grid-pattern p-type electrode using a metal shadow mask. The masked area is ~0.13 cm^2. For the n-type electrode, Ni (10 nm), Au-Ge (12%) (100 nm), Ni (30 nm), and Au (160 nm) are thermally evaporated onto the entire back surface, and rapidly thermally annealed in forming gas at 400 °C for 60 s. No anti-reflective coating or surface passivation is applied to these SCs. A typical SC has a device area of 0.5 cm^2.

4.1.3   Device characterisation

A Veeco Nanoscope V atomic force microscope (AFM) was used to characterise the morphology of an uncapped QD layer. Temperature-dependent and power-dependent PL spectra have been obtained using continuous-wave PL measurements performed using 532 nm excitation from a diode pumped solid-state laser. A cryostat was used to control the sample temperature between 10 and 300 K. Transient photoluminescence was examined using a 6 ns pulse at 505 nm from a Continuum Panther optical parametric oscillator (OPO) pumped with a Surelite-I laser. The sample was held at 80K in an Oxford Instruments Optistat continuous flow cryostat and the luminescence was dispersed in a Triax 550 spectrometer with a 600-lines/mm grating Blazed at 1µm. The luminescence was detected with a Hamamatsu R5509-72 photomultiplier and recorder using a LeCroy Waverunner-2 Oscilloscope. For electrical characterisation, J–V measurements have been performed under one-sun (AM 1.5G) illumination using a LOT calibrated solar simulator with a Xeon lamp. A 4-point probe station was used to connect the devices to a Keithly 2400 sourcemeter that outputs the data to Photor 3.1 software. Photocurrent measurements were obtained with a halogen lamp chopped to a frequency of 188 Hz through a Newport monochromator; a 4-point probe in connection with a lock-in amplifier was used to collect data. The calibration for the monochromatic

beam was performed using a Silicon photo-diode and the data was analysed with Tracer 3.2 software to produce the EQE spectra.

4.2   Results and discussion

4.2.1   Structural characterisation

A Veeco Nanoscope V atomic force microscope (AFM) was used to characterise the morphology of uncapped InAs QDs on GaAs interlayer, as shown in Figure 3.2. The average diameter of the QDs was measured to be ~ 40 nm, with an average height of ~ 6 nm. No large defected dots were observed and indicate a high structural quality [11]. The QD density per layer was estimated to be ~ 4.3×10^{10} cm^{-2}. Increasing the Sb composition in the GaAs$_{1-x}$Sb$_x$ QW did not have significant influence on the shape, size, and the density of the QDs, unlike Sb mediated QD growth [12].
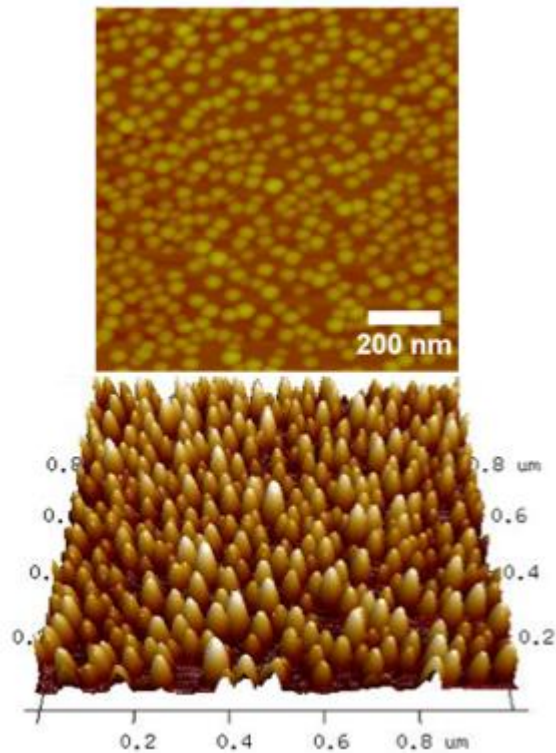
Figure 4.2. AFM images of InAs QDs grown on GaAs in 2D (top) and 3D (bottom).

4.2.2 Optical characterisation

Figure 4.3 (a) and (c) show the temperature-dependent PL spectra (20 - 300 K) and a schematic energy band diagram of the hybrid InAs-QD/GaAs$_{1-x}$Sb$_x$-QW SCs, respectively. At 300 K, the PL intensity for $x = 0.08$ to 0.17 drops by two orders of magnitude compared with $x = 0$. A reduction in QD peak intensity is an indicator of type-II band alignment due to the lower photon absorption efficiency. This behaviour is therefore expected for samples with $x = 0.14$ and 0.17.

Two peaks are observed for $x = 0.14$ and 0.17. At temperatures above 140 K, the intensity of the high-energy peak exceeds that of the low-energy peak. This is unusual because carriers are expected to easily transition to lower energy states at higher temperatures. As the temperature drops below 140 K, the low energy peak starts to dominate. This indicates a preferred emission pathway through a higher energy state at higher temperatures, which is inhibited at low temperatures.

Figure 4.3 (b) shows the log-scale power-dependent PL spectra of the hybrid solar cells measured at 10 K. The QD peak emission for $x = 0$ spans a wide range of wavelengths (900-1100 nm), which indicates a large size distribution of QDs is present. The GaAs peak can clearly be identified at ~830 nm. The GaAs peak is an order of magnitude higher for samples with Sb present. This can be linked to the conduction band offset (CBO) formed between the GaAs and GaAsSb QW. At 10 K, the electrons in the GaAs CB are inhibited by the CBO from transitioning to lower energy states in the QDs, thereby increasing GaAs peak emission. The onset of the QD peak emission is shown to red-shift with increasing Sb composition from 900 nm to 1000 nm. This is attributed to the increasing VBO between the QD and the QW for increasing Sb composition.

This behaviour is therefore expected for samples with $x = 0.14$ and 0.17. However, this does not explain the significant drop in intensity for $x = 0.08$, which has type-I band alignment. One explanation could be the formation of defects created by the lattice mismatch between the GaAsSb QW and GaAs interlayer. This is supported by the full recovery of the PL intensity at low temperatures (20 K), which reduces the carrier mobility and limits the contribution from non-radiative recombination centres. However, these defects could play a significant role in limiting device efficiency when performing electrical measurements. A drop in PL intensity for the $x = 0$ below 120 K can also be observed. This is attributed to the strain field between the InAs QDs and the GaAs interlayer/WL, which creates a potential barrier at the interface that decreases the carrier capture efficiency of QDs at low temperature. Also the quality of the interface between the GaAs and QDs require that trap states and non-radiative recombination centres be taken into consideration [13].
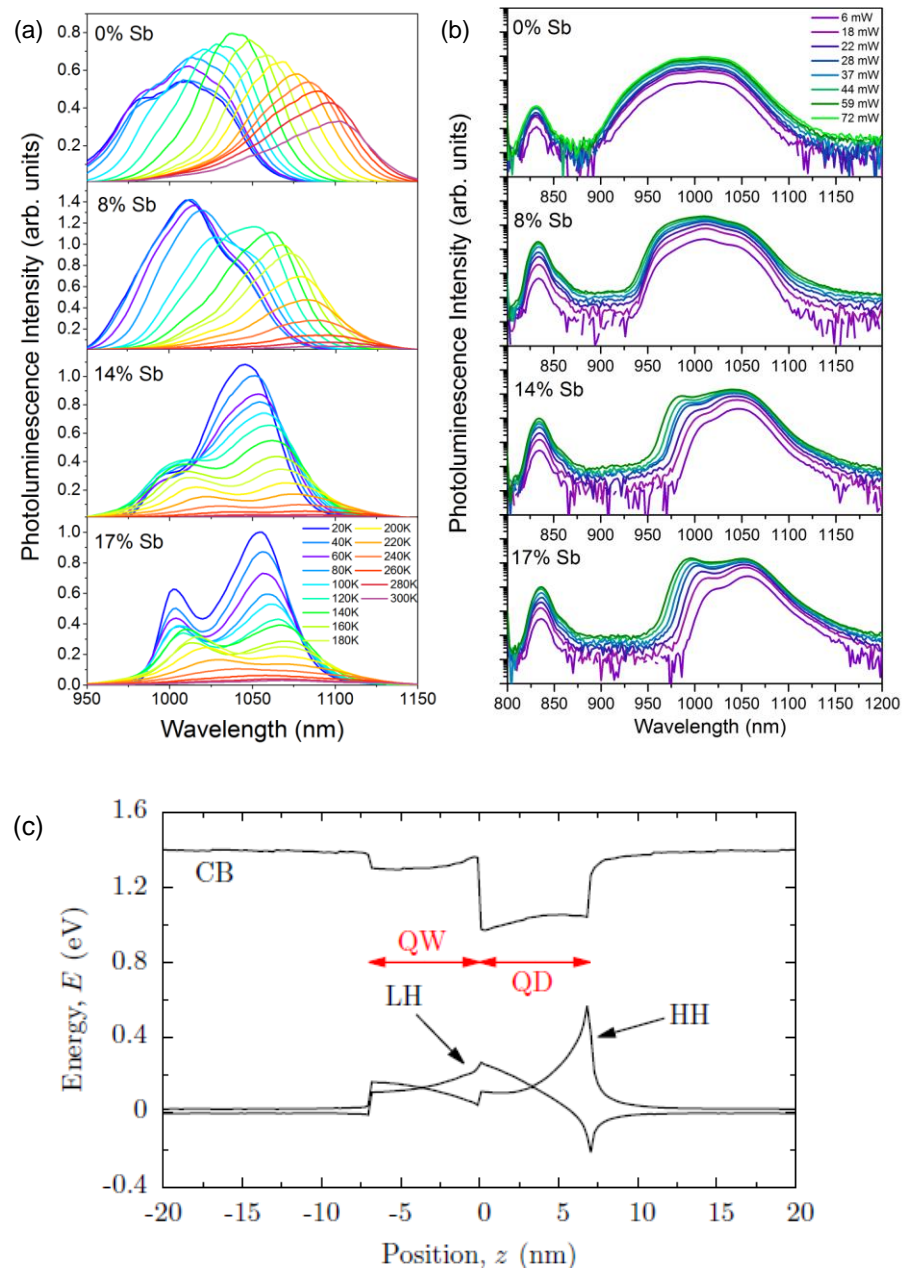
Figure 4.3. Photoluminescence spectra of hybrid InAs-QD/GaAs$_{1-x}$Sb$_x$-QW SCs (x = 0, 0.08, 0.14, and 0.17) showing (a) linear-scale temperature-dependent measurements at 37mW laser excitation, (b) semi-log scale laser excitation power-dependent measurements at 10K, and (c) a schematic energy band diagram of the InAs-QD/GaAs$_{0.83}$Sb$_{0.17}$-QW structure.
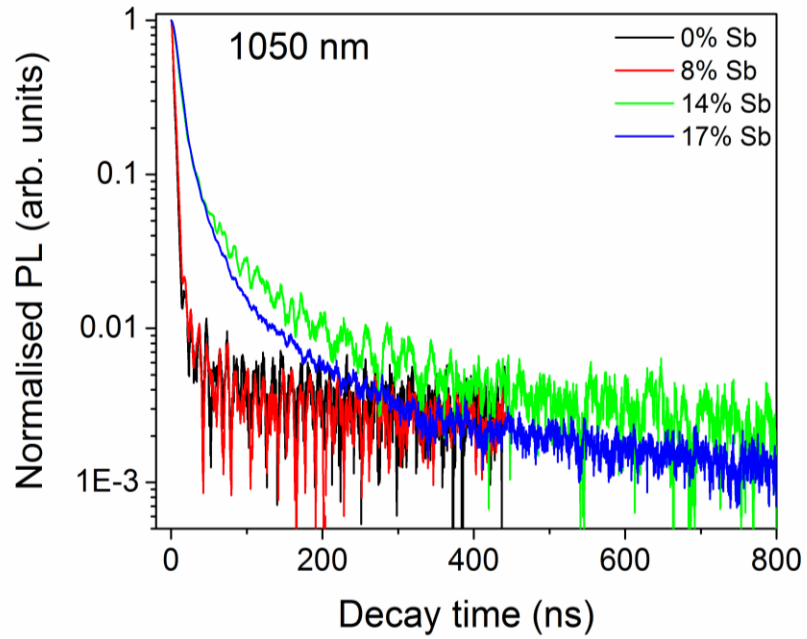
Figure 4.4. Normalised PL intensity vs. decay time at 1050 nm emission from time resolved PL measurements for InAs-QD/GaAs$_{1-x}$Sb$_x$-QW SCs (x = 0, 0.08, 0.14, and 0.17) at 80 K.
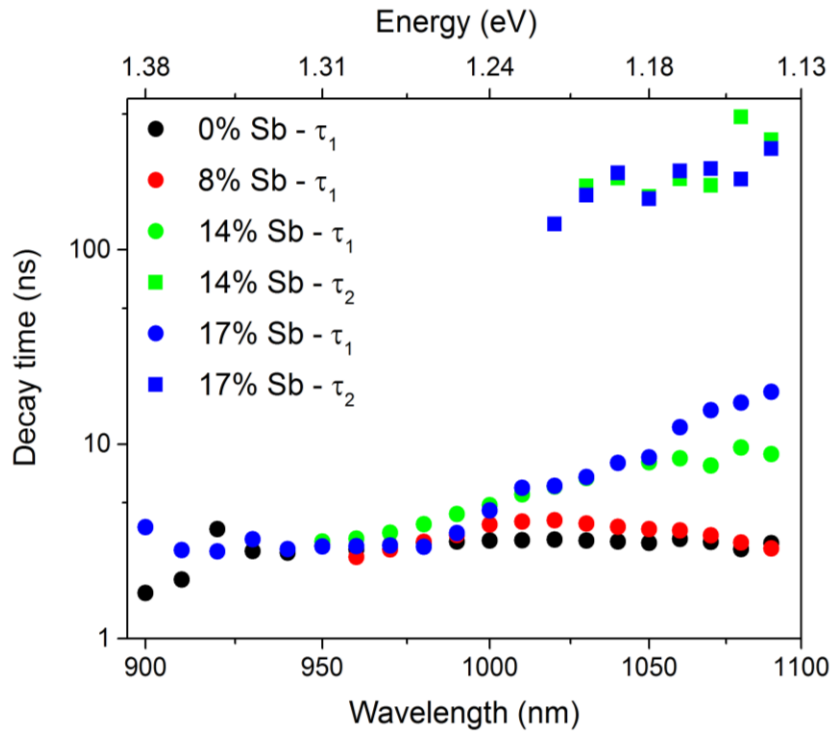
Figure 4.5. Carrier decay time vs. emission wavelength from time resolved PL measurements for InAs-QD/GaAs$_{1-x}$Sb$_x$-QW SCs (x = 0, 0.08, 0.14, and 0.17) at 80 K.

Figure 4.4 shows the decay times of the hybrid InAs-QD/GaAs$_{1-x}$Sb$_x$ –QW SCs measured at 1050 nm emission. Both x = 0 and 0.08 show decays times comparable to that of the laser (~3ns), confirming type-I behaviour. Whereas significantly prolonged carrier lifetimes approaching 480 ns were measured for the samples with x = 0.14 and x = 0.17 [14]. This exceeds previously reported type-II carrier lifetimes by almost two-and-half times. A double exponential decay fitting is used to calculate the carrier lifetimes across the 900-1100 nm spectra, as shown in Equation 4.1.

$$y = y_0 + A_1 e^{-\frac{t}{\tau_1}} + A_2 e^{-\frac{t}{\tau_2}},$$

Figure 4.5 shows the type-II SCs have two distinct carrier lifetimes, 5 - 15 ns and 100-500 ns. Figure 4.6 shows the absolute PL intensity plotted against the emission wavelength to determine the peak contribution for each decay time. The fast decay (τ_1) and slow decay (τ_2) times are represented by square and circle symbols, respectively. Figure 4.6 shows $x = 0.14$ (green) has peaks at $\tau_1 \sim$ 1050 nm and $\tau_2 \sim$ 1055 nm, while $x = 0.17$ has two peaks at $\tau_1 \sim 990$ and 1060 nm, and one at $\tau_2 \sim$ 1080 nm. The separation of charge carriers gives rise to the band bending in the GaAsSb-QW. This is predicted to create a potential well (H_0) close to the QW/GaAs-interlayer interface, and a second energy state (H_1) across the QW region. The QD electron ground state E_0 has a narrower wavefunction than the excited state E_1 due to the deeper confinement. The overlap of these electron-hole wavefunctions determines the possible emission pathways and explains the two different decay times. Due to the spatial separation of charge carriers in the type-II SCs, the selection rules start to break down and allow new emission pathways to exist [6], [15]. However, the new emission pathways, E_0H_1 and E_1H_0, are expected to be weaker.
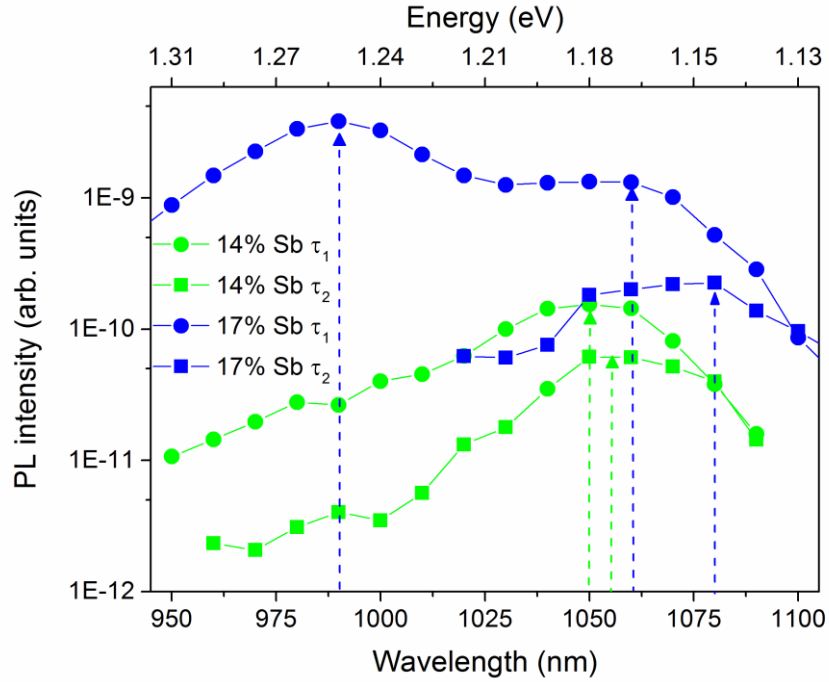
Figure 4.6. Absolute PL intensity contributions of the different decay components for InAs-QD/GaAs$_{1-x}$Sb$_x$-QW SCs (x = 0.14 and 0.17) at 80 K.

By examining the e$^-$/h$^+$ wavefunctions overlap, the shorter carrier lifetime, τ_1, is assigned to E$_1$H$_0$ and E$_1$H$_1$, while the prolonged carrier lifetime, τ_2, originates from E$_0$H$_1$ and E$_0$H$_0$ emission. H$_1$ has greater sensitivity to band bending than H$_0$ due to the electric field accumulating holes close to the GaAsSb-QW/GaAs interlayer interface. This also explains the two peaks energies for $x = 0.14$ and 0.17 that do not shift with increasing laser excitation power, E$_0$H$_0$ and E$_1$H$_0$. This is further evidenced by the temperature-dependent PL that showed for T >140 K, the excited state QD emission is more favourable than the ground state. However, below 140 K,

electrons can no longer thermally escape to E_1 and E_0 emission starts to dominate. In addition, previously reported power-dependent TRPL for a similar structure show that carrier lifetime increases with decreasing excitation intensity [14]. This supports the suggested theory, as fewer carriers will be promoted to the higher energy states that lead to the faster decay transitions. The GaAs interlayer therefore serves to further restrict the e^-/h^+ wavefunction overlap and prolong the carrier lifetime beyond that of InAs-QD/GaAsSb-QW SCs without the GaAs interlayer.

4.2.3 Solar cell performance characterisation

Current density vs. voltage (J-V) measurements were performed on the hybrid InAs-QDs/GaAs$_{1-x}$Sb$_x$-QW SCs with GaAs interlayer as shown in Figure 4.7. The short-circuit current density (J_{SC}), open-circuit voltage (V_{OC}), fill factor (FF) and efficiency (η) are derived from the J-V plot and presented in Table 4.1. The earlier study showed a significant reduction in J_{SC} with increasing Sb composition [7]. It is clear that by inserting a GaAs interlayer into the hybrid SC structure, a high J_{SC} of 18.0 mA cm^{-2} can be achieved for the x= 0.14 and 0.17 SCs. Although this J_{SC} is 0.4 mA cm^{-2} higher than the reference x = 0 type-I QDSC, the overall efficiency is 2.5% lower due to the drop in V_{OC}.
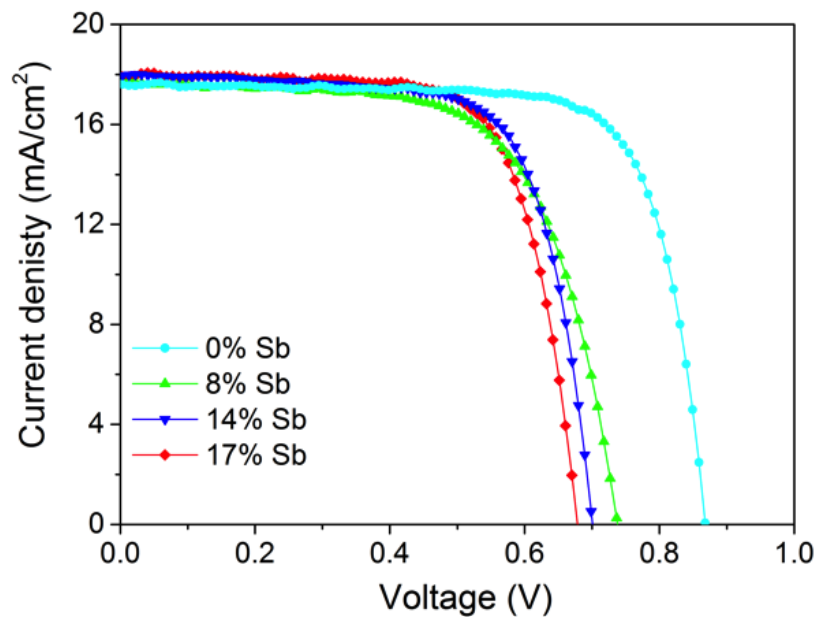
Figure 4.7. Current-density vs. voltage plot of InAs QDs/GaAs interlayer/GaAs$_{1-x}$Sb$_X$ QW solar cells for x = 0, 0.08, 0.14 and 0.17. Measurements were conducted under one sun with global AM 1.5 illumination at room temperature.

Table 4.1 Short-circuit current density (J_{SC}), open-circuit voltage (V_{OC}), fill factor (FF) and efficiency (η) derived from the J-V plot in Figure 5.

Device	J_{SC} (mA cm^{-2})	V_{OC} (V)	FF (%)	η (%)
0 Sb	17.6	0.86	75.4	11.5
0.08 Sb	17.7	0.74	65.5	8.6
0.14 Sb	18.0	0.70	71.3	9.0
0.17 Sb	18.0	0.68	71.4	8.7

As with the previous study, the drop in V_{OC} is prevalent as shown in Figure 4.7. The V_{OC} is primarily governed by the bandgap energy and recombination current of the SC. A difference of 0.18 V between $x = 0$ to 0.17 is too large to be solely due to the reduction in bandgap energy. This is supported by the significant drop in V_{OC} observed for $x = 0.08$, which has type-I band alignment and should not have an effect on the bandgap energy. Therefore, as indicated by the reduction in temperature-dependent PL intensity in Figure 4.3, the non-radiative recombination centres play a significant role in limiting the overall device efficiency. This can be assigned to a high density of strain-induced dislocations that reduce minority carrier lifetime and diffusion length. Introducing rapid thermal annealing to remove the point defects or potentially Si-doping the QDs to increasing QD confinement could recover the V_{OC} [16], [17].
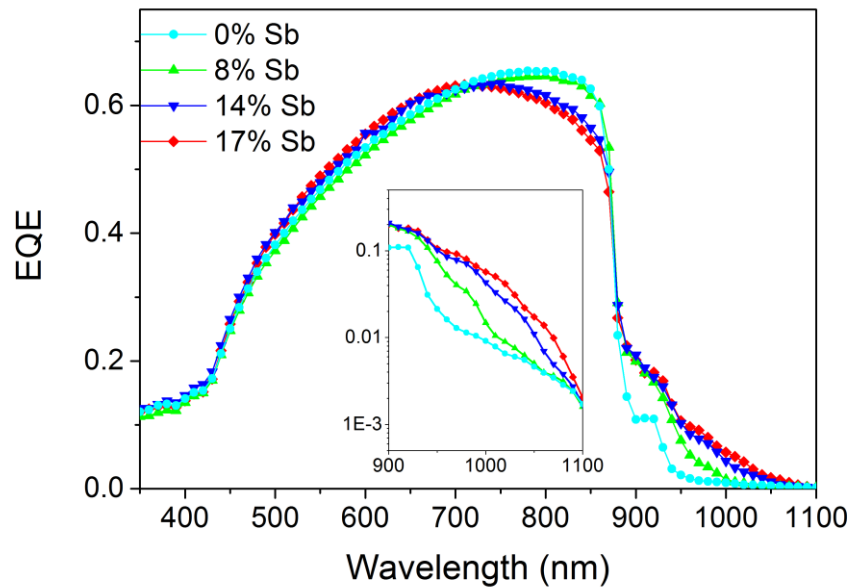
Figure 4.8. Linear-scale external quantum efficiency spectra of a GaAs reference solar cell and InAs QDs/GaAs interlayer/GaAs$_{1-x}$Sb$_x$ QW solar cells, where x = 0, 0.08, 0.14 and 0.17. The inset shows an enlarged semi-log scale plot that corresponds to the QD region.

The EQE spectra in Figure 4.8 demonstrate the photocurrent generated between 350-1100 nm at zero-bias and is directly related to the J_{SC} measured in Figure 4.7. In the absence of an anti-reflective coating and passivation layer, the EQE shows a limited photo-response for higher photon energies (350-500 nm) that are collected close to the surface. Between 700-900 nm, the EQE for type-I ($x < 0.14$) and type-II ($x \geq 0.14$) band alignment can be clearly distinguished. The insertion of the GaAs interlayer has shown it can greatly improve the EQE in this region by increasing the QW confinement and therefore lowering the potential barrier for holes to transition to the VB. However, the introduction of strained

GaAsSb layers is likely to degrade the material quality, which leads to increased non-radiative recombination and lower EQE observed between 700-900 nm. It is worth noting that IBSCs are designed to operate under concentrated illumination (i.e. 500 suns) where a high density of charge carriers will be generated. Hence, the restrictions to hole transport across the QW will be minimised as the hole concentration in the QW increases and further lowers the VB potential barrier.

The inset of Figure 4.7 shows the semi-log scale plot of the WL and QD region. In the QD region (950-1100 nm) an order of magnitude improvement in EQE can be observed between the $x = 0$ and 0.17. This can be credited to both the significantly prolonged carrier lifetime associated with the type-II band alignment, and the improved hole transport across the active region generated by the GaAs interlayer.

4.3　Conclusion

In summary, hybrid InAs-QD/GaAs$_{1-x}$Sb$_x$-QW SCs (x = 0, 0.08, 0.14, and 0.17) with a GaAs interlayer were studied. Type-II band alignment was demonstrated using power-dependent PL measurements for the samples with x = 0.14 and x = 0.17 and prolonged carrier lifetime up to 480ns was shown by transient PL measurements. The prolonged lifetime was attributed to the GaAs interlayer that served to further reduce the e$^-$/h$^+$ wavefunction overlap of the type-II structure. Both x = 0.14 and 0.17 exhibited a high J$_{SC}$ of 18.0 mA cm^{-2} with efficiency of 9.0 and 8.7% respectively. EQE measurements confirmed the improvement in J$_{SC}$ is due to the increased photocurrent contribution from the QD region. This is linked to the prolonged lifetime associated with the type-II band alignment and the insertion of the GaAs interlayer. This provides a mean to overcome the challenges related to the short carrier lifetime of type-I QD-IBSCs.

4.4 References

[1] W.-S. Liu, Y.-T. Wang, W.-Y. Qiu, and C. Fang, 'Carrier Dynamics of a Type-II Vertically Aligned InAs Quantum Dot Structure with a GaAsSb Strain-Reducing Layer', *Appl. Phys. Express*, vol. 6, no. 8, p. 085001, Aug. 2013.

[2] S. Tomić, 'Effect of Sb induced type II alignment on dynamical processes in InAs/GaAs/GaAsSb quantum dots: Implication to solar cell design', *Appl. Phys. Lett.*, vol. 103, no. 7, p. 072112, Aug. 2013.

[3] R. B. Laghumavarapu *et al.*, 'GaSb/InGaAs quantum dot–well hybrid structure active regions in solar cells', *Sol. Energy Mater. Sol. Cells*, vol. 114, pp. 165–171, Jul. 2013.

[4] H. Y. Liu *et al.*, 'Long-wavelength light emission and lasing from InAs⁄GaAs quantum dots covered by a GaAsSb strain-reducing layer', *Appl. Phys. Lett.*, vol. 86, no. 14, p. 143108, Apr. 2005.

[5] K.-Y. Ban, D. Kuciauskas, S. P. Bremnerand, and C. B. Honsberg, 'Determination of a Sb composition in InAs/GaAsSb for negligible valence band offset', in *2010 35th IEEE Photovoltaic Specialists Conference (PVSC)*, 2010, pp. 003306–003309.

[6] K.-Y. Ban, D. Kuciauskas, S. P. Bremner, and C. B. Honsberg, 'Observation of band alignment transition in InAs/GaAsSb quantum dots by photoluminescence', *J. Appl. Phys.*, vol. 111, no. 10, p. 104302, May 2012.

[7] S. Hatch *et al.*, 'InAs/GaAsSb quantum dot solar cells', *Opt. Express*, vol. 22, no. S3, pp. A679–A685, May 2014.

[8] F. K. Tutu *et al.*, 'Improved performance of multilayer InAs/GaAs quantum-dot solar cells using a high-growth-temperature GaAs spacer layer', *J. Appl. Phys.*, vol. 111, no. 4, p. 046101, Feb. 2012.

[9] H. Y. Liu *et al.*, 'Influences of the spacer layer growth temperature on multilayer InAs⁄GaAs quantum dot structures', *J. Appl. Phys.*, vol. 96, no. 4, pp. 1988–1992, Aug. 2004.

[10] H. Y. Liu *et al.*, 'Improved performance of 1.3μm multilayer InAs quantum-dot lasers using a high-growth-temperature GaAs spacer layer', *Appl. Phys. Lett.*, vol. 85, no. 5, pp. 704–706, Aug. 2004.

[11] H. Y. Liu *et al.*, 'p-doped 1.3μmInAs⁄GaAs quantum-dot laser with a low threshold current density and high differential efficiency', *Appl. Phys. Lett.*, vol. 89, no. 7, p. 073113, Aug. 2006.

[12] F. K. Tutu *et al.*, 'Antimony mediated growth of high-density InAs quantum dots for photovoltaic cells', *Appl. Phys. Lett.*, vol. 103, no. 4, p. 043901, Jul. 2013.

[13] D. P. Popescu, P. G. Eliseev, A. Stintz, and K. J. Malloy, 'Temperature dependence of the photoluminescence emission from InAs quantum dots in a strained Ga 0.85 In 0.15 As quantum well', *Semicond. Sci. Technol.*, vol. 19, no. 1, p. 33, 2004.

[14] K. Nishikawa *et al.*, 'Extremely long carrier lifetime over 200 ns in GaAs wall-inserted type II InAs quantum dots', *Appl. Phys. Lett.*, vol. 100, no. 11, p. 113105, Mar. 2012.

[15] C. Y. Jin *et al.*, 'Optical transitions in type-II InAs⁄GaAs quantum dots covered by a GaAsSb strain-reducing layer', *Appl. Phys. Lett.*, vol. 91, no. 2, p. 021102, Jul. 2007.

[16] P. Lam *et al.*, 'Voltage recovery in charged InAs/GaAs quantum dot solar cells', *Nano Energy*, vol. 6, pp. 159–166, May 2014.

[17] P. Lam *et al.*, 'The Effect of Rapid Thermal Annealing on InAs/GaAs Quantum Dot Solar Cells', *IET Optoelectron.*, 2014.

Chapter 5

The influence of delta doping and modulation doping on InAs/GaAs quantum dot solar cells

One of the main challenges in implementing high-efficiency QD IBSCs is to prevent the decrease in V_{OC} when QDs are introduced to the structure. The V_{OC} drop originates from the thermal coupling between IB and conduction band (CB) that occurs when carriers can be thermally excited and relaxed between IB and CB, and hence, there is no need for two-photon excitation. Studies have suggested possible solutions to prevent the V_{OC} drop [1]–[3]. Amongst those, Okada *et al.* demonstrated the two-photon absorption via intermediate quantum states in InAs/GaNAs QD IBSC at room temperature by direct Si-doping of QDs [1]. However, to date, there has been no published study comparing IB QDSCs with different types and the positions of Si doping.

In this project, five QDSCs with different doping methods and positions, alongside two reference cells, have been grown by MBE and characterised by photoluminescence (PL), external quantum efficiency (EQE), and J – V measurements.

Three doping methods investigated in this work are direct doping, delta doping, and modulation doping. Firstly, Si direct doping is a doping method that creates a built-in field at the interface between the QDs and wetting layer (WL) by direct Si doing in QDs. The built-in energy formed at the QDs/WL interface increases the thermal activation energy, which leads to a reduced thermal activity from IB to CB [4]. It is believed that Si direct doping can help achieve voltage recovery without employing higher bandgap material. Secondly, it is believed that Si delta doping embedded into intrinsic spacer the QDs can improve sub bandgap collection efficiency [5]. With delta-doped QDs, the confined states between CB and VB are already partially filled with carriers. Therefore, it is possible for photons with sub bandgap energy to help carriers transit into CB continuum. Sablon *et al*. have demonstrated an increased sub bandgap current collection after the introduction of delta doing [6], whereas others observed carrier extraction through two-photon sequential absorption [1], [7]. Also, Morioka *et al*. have shown that band flattened by delta-doped QDs significantly reduces Shockley-Read-Hall (SRH) recombination rate and dark current [8].

Lastly, Si modulation doping is a doping method where doping is introduced in a thin spacer layer between QD layers [9].

5.1   Experimental work

5.1.1   Growth details

5.1.1.1   Reference SC - GaAs SC (R3)

The GaAs reference SC sample was grown by a solid-source molecular beam epitaxy (MBE) on n+ GaAs (100) substrates. As shown in

Figure 5.1, the GaAs reference SCs was grown with the same p-i-n structure that consists of a 200 nm GaAs buffer layer with Si doping density of 1×10^{18} cm^{-3}, 30 nm Al$_{0.33}$Ga$_{0.67}$As back surface field (BSF) with Si doping density of 1×10^{18} cm^{-3}, 420 nm intrinsic region GaAs, 1000 nm GaAs base with Si doping density of 1×10^{17} cm^{-3}, 250 nm GaAs emitter with Be doping density of 2×10^{18} cm^{-3}, 30 nm Al$_{0.6}$Ga$_{0.4}$As window layer with Be doping density of 2×10^{18} cm^{-3}, and 50 nm GaAs contact layer with Be doping density of 1×10^{19} cm^{-3}.

50 nm p+ GaAs	[Be: 1×10^{19} cm^{-3}]
30 nm p Al$_{0.6}$Ga$_{0.4}$As window	[Be: 2×10^{18} cm^{-3}]
250 nm p GaAs emitter	[Be: 2×10^{18} cm^{-3}]
420 nm i GaAs	
1000 nm n$^-$ GaAs base	[Si: 1×10^{17} cm^{-3}]
30 nm n+ Al$_{0.33}$Ga$_{0.67}$As BSF	[Si: 1×10^{18} cm^{-3}]
200 nm n+ GaAs buffer	[Si: 1×10^{18} cm^{-3}]
n+ GaAs (001) substrate	

Figure 5.1 Structure of GaAs Reference SC

5.1.1.2   Reference SC - Undoped GaAs/InAs QDSC (R4)

The reference QDSC sample has an identical structure to the reference GaAs SC except for its intrinsic region, as shown in

Figure 5.2. The intrinsic region of the undoped QDSC consists of 20 stacks of 2.1 monolayer (ML) InAs separated by a 20 nm GaAs spacer. The QDs were grown by the Stranski-Krastanov mode at substrate temperature of ~ 500 °C. High-growth-temperature GaAs spacer layers were applied during the growth of QDs to suppress the formation of dislocations [10]–[12].

50 nm p$^+$ GaAs	[Be: 1 × 10^{19} cm^{-3}]
30 nm p Al$_{0.75}$Ga$_{0.25}$As window	[Be: 2 × 10^{18} cm^{-3}]
250 nm p GaAs emitter	[Be: 2 × 10^{18} cm^{-3}]
16 nm i GaAs	
4 nm i GaAs	
▲▲▲▲▲▲▲▲▲▲▲▲▲▲▲▲▲▲▲▲▲▲▲▲▲▲▲▲	
20 nm i GaAs	2.3 ML InAs QDs ↲
1000 nm n$^-$ GaAs base	[Si: 1 × 10^{17} cm^{-3}]
30 nm n$^+$ Al$_{0.35}$Ga$_{0.65}$As BSF	[Si: 1 × 10^{18} cm^{-3}]
200 nm n$^+$ GaAs buffer	[Si: 1 × 10^{18} cm^{-3}]
n$^+$ GaAs (001) substrate	

× 20

Figure 5.2 Structure of undoped Reference QDSC

5.1.1.3 Doped InAs/GaAs QDSC - 8e/dot direct doping (R5)

The same QDSC structure as the undoped reference QDSC was used for directly doped QDSC reference QDSC except for the QD layers, as shown in Figure 5.3 During the QD growth, Si-dopants were directly introduced with doping density of 8 electrons per QD [4].

50 nm p$^+$ GaAs	[Be: 1×10^{19} cm^{-3}]
30 nm p Al$_{0.75}$Ga$_{0.25}$As window	[Be: 2×10^{18} cm^{-3}]
250 nm p GaAs emitter	[Be: 2×10^{18} cm^{-3}]
16 nm i GaAs	
4 nm i GaAs	Direct Si doping (8 e/dot) ↴
▲▲▲▲▲▲▲▲▲▲▲▲▲▲▲▲▲▲▲▲▲▲▲▲▲▲▲▲▲▲	
20 nm i GaAs	2.3 ML InAs QDs ↱
1000 nm n$^-$ GaAs base	[Si: 1×10^{17} cm^{-3}]
30 nm n$^+$ Al$_{0.35}$Ga$_{0.65}$As BSF	[Si: 1×10^{18} cm^{-3}]
200 nm n$^+$ GaAs buffer	[Si: 1×10^{18} cm^{-3}]
n$^+$ GaAs (001) substrate	

× 20

Figure 5.3 Structure of directly doped (8 e/dot) QDSC

5.1.1.4   Doped InAs/GaAs QDSC - 8e/dot delta-doping (R6 and R7)

In order to study the effect of delta-doping and its position dependence in QDSCs for delta-doping study, Si delta-doping was introduced above the QD layers for R6 sample, and below the QD layers for R7 sample, as shown in Figure 5.4 and Figure 5.5.

50 nm p+ GaAs	[Be: 1×10^{19} cm^{-3}]
30 nm p Al$_{0.75}$Ga$_{0.25}$As window	[Be: 2×10^{18} cm^{-3}]
250 nm p GaAs emitter	[Be: 2×10^{18} cm^{-3}]
13 nm i GaAs	
3 nm i GaAs	Si delta-doping (8 e/dot) ↱
4 nm i GaAs	
▲▲▲▲▲▲▲▲▲▲▲▲▲▲▲▲▲▲▲▲▲▲▲▲▲▲▲	
20 nm i GaAs	2.3 ML InAs QDs ↲
1000 nm n- GaAs base	[Si: 1×10^{17} cm^{-3}]
30 nm n+ Al$_{0.35}$Ga$_{0.65}$As BSF	[Si: 1×10^{18} cm^{-3}]
200 nm n+ GaAs buffer	[Si: 1×10^{18} cm^{-3}]
n+ GaAs (001) substrate	

× 20

Figure 5.4 Structure of delta-doped QDSC (above QDs)

50 nm p+ GaAs	[Be: 1×10^{19} cm^{-3}]
30 nm p Al$_{0.75}$Ga$_{0.25}$As window	[Be: 2×10^{18} cm^{-3}]
250 nm p GaAs emitter	[Be: 2×10^{18} cm^{-3}]
3 nm i GaAs	
13 nm i GaAs	
4 nm i GaAs	
▲▲▲▲▲▲▲▲▲▲▲▲▲▲▲▲▲▲▲▲▲▲▲▲▲▲▲	
3 nm i GaAs	2.3 ML InAs QDs ↲
17 nm i GaAs	Direct Si doping (8 e/dot) ↲
1000 nm n- GaAs base	[Si: 1×10^{17} cm^{-3}]
30 nm n+ Al$_{0.35}$Ga$_{0.65}$As BSF	[Si: 1×10^{18} cm^{-3}]
200 nm n+ GaAs buffer	[Si: 1×10^{18} cm^{-3}]
n+ GaAs (001) substrate	

× 20

Figure 5.5 Structure of delta-doped QDSC (below QDs)

5.1.1.5 Doped InAs/GaAs QDSC - 8e/dot modulation-doping (R8 and R9)

The influence of modulation doping and its position dependence on QDSCs could be investigated by introducing 6 nm thick modulation-doped layers below (R8) and above (R9) the QD layers, as shown in Figure 5.6 and Figure 5.7.

50 nm p$^+$ GaAs	[Be: 1 × 10^{19} cm^{-3}]
30 nm p Al$_{0.75}$Ga$_{0.25}$As window	[Be: 2 × 10^{18} cm^{-3}]
250 nm p GaAs emitter	[Be: 2 × 10^{18} cm^{-3}]
9 nm i GaAs	
7 nm i GaAs	
4 nm i GaAs	
▲▲▲▲▲▲▲▲▲▲▲▲▲▲▲▲▲▲▲▲▲▲▲▲▲▲▲▲▲	
3 nm i GaAs	2. 3 ML InAs QDs ↵
6 nm i GaAs	Si modulation doping (8 e/dot)
11 nm i GaAs	
1000 nm n$^-$ GaAs base	[Si: 1 × 10^{17} cm^{-3}]
30 nm n$^+$ Al$_{0.35}$Ga$_{0.65}$As BSF	[Si: 1 × 10^{18} cm^{-3}]
200 nm n$^+$ GaAs buffer	[Si: 1 × 10^{18} cm^{-3}]
n$^+$ GaAs (001) substrate	

× 20

Figure 5.6 Structure of modulation-doped QDSC (below QDs)

50 nm p+ GaAs	[Be: 1×10^{19} cm^{-3}]	
30 nm p Al$_{0.75}$Ga$_{0.25}$As window	[Be: 2×10^{18} cm^{-3}]	
250 nm p GaAs emitter	[Be: 2×10^{18} cm^{-3}]	
7 nm i GaAs		
6 nm i GaAs	Si modulation doping (8 e/dot)	× 20
3 nm i GaAs		
4 nm i GaAs		
▲▲▲▲▲▲▲▲▲▲▲▲▲▲▲▲▲▲▲▲▲▲▲▲▲▲▲▲		
20 nm i GaAs	2. 3 ML InAs QDs ↲	
1000 nm n- GaAs base	[Si: 1×10^{17} cm^{-3}]	
30 nm n+ Al$_{0.35}$Ga$_{0.65}$As BSF	[Si: 1×10^{18} cm^{-3}]	
200 nm n+ GaAs buffer	[Si: 1×10^{18} cm^{-3}]	
n+ GaAs (001) substrate		

Figure 5.7 Structure of modulation-doped QDSC (above QDs)

5.1.2　Device processing

For the sample cleaning, the SCs were ultrasonicated first in acetone and then in isopropanol for 10 min each. The surface oxide removal was performed by immersing the SCs in dilute ammonia solution (1:19) for 30 s. A Au-Zn alloy (95 % Au, 5 % Zn) was thermally evaporated to form a (~ 200 nm thick) grid-pattern p-type electrode using a metal shadow mask. For the n-type electrode, 10 nm Ni, 100 nm Au-Ge (88 % Au, 12 % Ge), 30 nm Ni, and 200 nm Au were thermally evaporated onto the entire back surface, and thermally annealed at 400 °C for 60 s. No anti-reflective coating or surface passivation was applied to these SCs.

5.1.3 Device characterisation

A Veeco Nanoscope V atomic force microscope (AFM) was used to characterise the morphology of an uncapped QD layer. Temperature-dependent and power-dependent photoluminescence (PL) measurements were performed using 532 nm excitation from a diode-pumped solid-state laser. The sample temperature between 10 K and 300 K was controlled using a He-cooled cryostat during the PL measurements. Current density vs voltage (J-V) characteristics were obtained by using an LOT calibrated solar simulator with a xenon lamp under one-sun air mass (AM) 1.5 G illumination at room temperature. A 4-point probe station was used to connect devices to a Keithly 2400 sourcemeter that outputs the data to ReRa Tracer 3 software. Photocurrent measurements were performed with a halogen lamp chopped to a frequency of 188 Hz through a Newport monochromator. The monochromatic beam was calibrated with a silicon photo-diode and the data was analysed with ReRa Photor QE 3.1 software to obtain the external quantum efficiency (EQE) at room temperature.

5.2 Results and discussion

5.2.1 Structural characterisation

Figure 5.8 shows the AFM image of the InAs/GaAs QDSC. The average diameter of the QDs was measured to be ~ 30 nm, with an average height of ~ 5 nm. No large defective clusters were observed, which indicates a high structural quality [13]. The dot density was estimated to be ~ 3.35 × 10^{10} cm^{-2}.
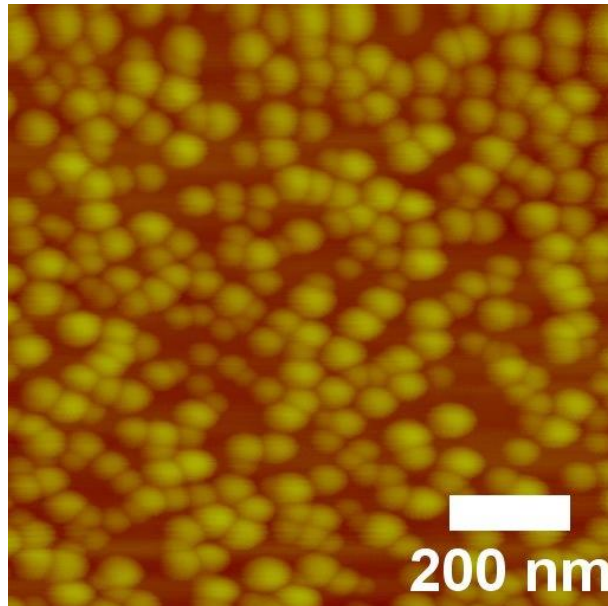

Figure 5.8 AFM images of InAs QDs grown on GaAs ($1 \times 1 \mu m^2$)

5.2.2 Optical characterisation

Figure 5.9 and Figure 5.10 show the PL spectra and the integrated PL intensities for all QDSC samples (R4 – R9) at rom temparature (300 K). All samples display two peaks at ~950 nm and ~1100 nm which correspond to the emissions from the WL and the QD ground state, respectively. Improved PL intensity is observed for the directly doped QDSC sample (R5) compared with the undoped QDSC sample (R4). This enhanced PL emission suggest that PL quenching is suppressed due to an increased thermal activation energy. The increase in the thermal activation energy is attributed to the potential barrier between GaAs and the QDs formed by Si doping, as demonstrated by Lam et al. [4]. This potential barrier can suppress the thermal escape of electrons from QDs, and hence contribute to the recovery of V_{OC}. A further increase in the PL intensity are observed for the delta-doped QDSC samples (R6 and R7). When Si doping is introduced within QDs, the presence of the Si atoms can lead to the destruction of the crystal lattice, and hence introduce non-radiative recombination centres [14]. However, it has been reported that placing dopants away from the QDs can reduce the number of point defects in the active QD region [15]. The increase in the PL emissions of the delta-doped QDSC samples suggests that delta doping accompanies less crystal lattice destruction as the Si dopants are introduced above/below the QDs rather

than inside the QDs, which means smaller number of non-radiative recombination centres in presence.
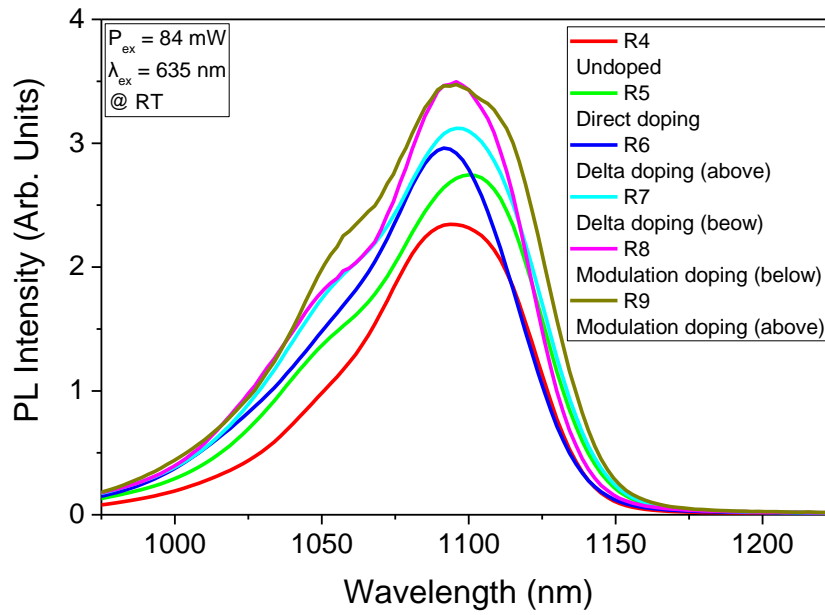

Figure 5.9 PL spectra of QDSC samples (R4 – R9). (P_{ex} = 84 mW and λ_{ex} = 635 nm at room temperature).
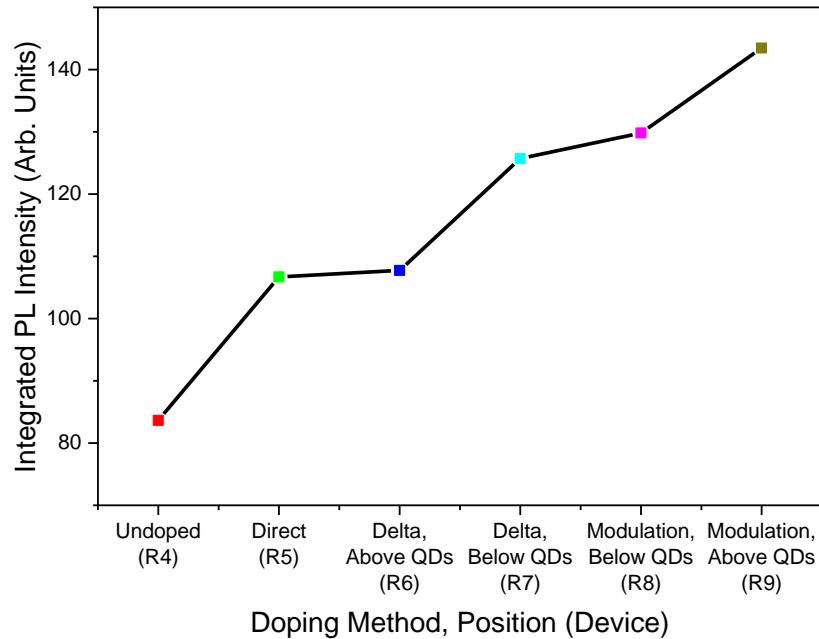
Figure 5.10 Integrated PL intensity vs. Si doping method and position at room temperature (P_{ex} = 84 mW, λ_{ex} = 635 nm).

The highest integrated PL intensity is observed for the modulation-doped QDSC samples (R8 and R9). This could be because of the presence of the 7 nm GaAs spacer layer between the Si-doped layer and the QD layer. In other words, the introduction the Si dopants could have a less significant influence on the morphology of the QDs during the growth as the QDs are separated from the Si-doped layer.

The full width at half maximum (FWHM) for R4 to R9 are Shown below in Figure 5.11. The similar linewidths of R4-R9 indicate that the Si doping does not significantly affect the size distribution of the QDs.
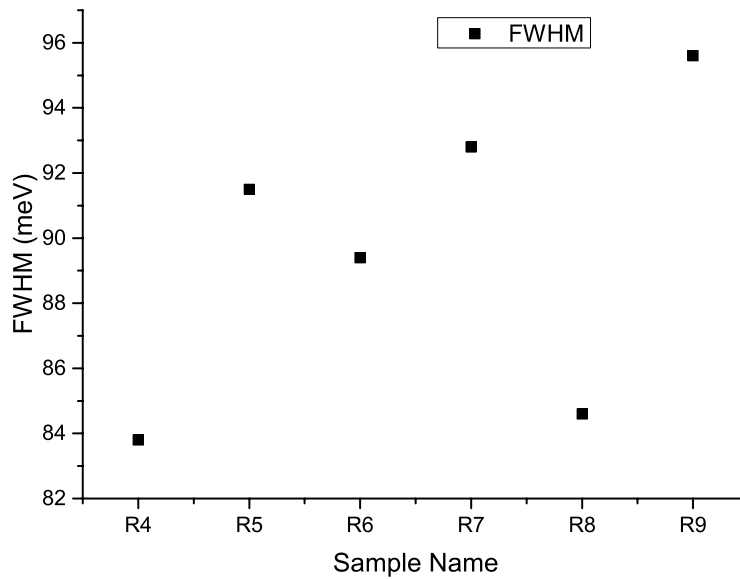
Figure 5.11 FWHM of R4 to R9 with excitation power of 28mW at room temperature.

To summarise, the results from the PL measurements show a clear correlation between the degree of separation between the Si dopants and the QDs, and the number of non-radiative recombination centres. In the QDSC with direct doping, the Si dopants are embedded in the QDs, which leads to the introduction of defects and non-radiative recombination centres [14]. Using delta doping could reduce the introduction of defects by avoiding the direct embedment of the Si dopants. A further reduction is achieved by the modulation doping, where the Si atoms are physically separated from the QDs by 7 nm GaAs spacer layer.

5.2.3 Solar cell performance characterisation

Figure 5.12 illustrates the EQE spectra of all SC samples. It shows that all SCs with Si doping (direct, delta, and modulation) have lower spectral response in the GaAs region (400 nm – 900 nm). This can be attributed to the decrease in depletion region after Si doping, which reduces the effective absorption area. For all QDSCs, sub-bandgap photons absorption is observed in the range from 900 nm to 1100 nm. All Si-doped samples display reduced spectral response in the sub-bandgap region. This is primarily attributed to the extra electrons introduced by Si doping filling the CB of the QDs, which decreases the probability of the VB to IB transition. As a result, the absorption from the QDs is weakened [14]. Another possibility for the reduced EQE is the suppression of thermal escape of photo-excited carriers due to the formation of a potential barrier at QD/WL interface by Si doping [4].
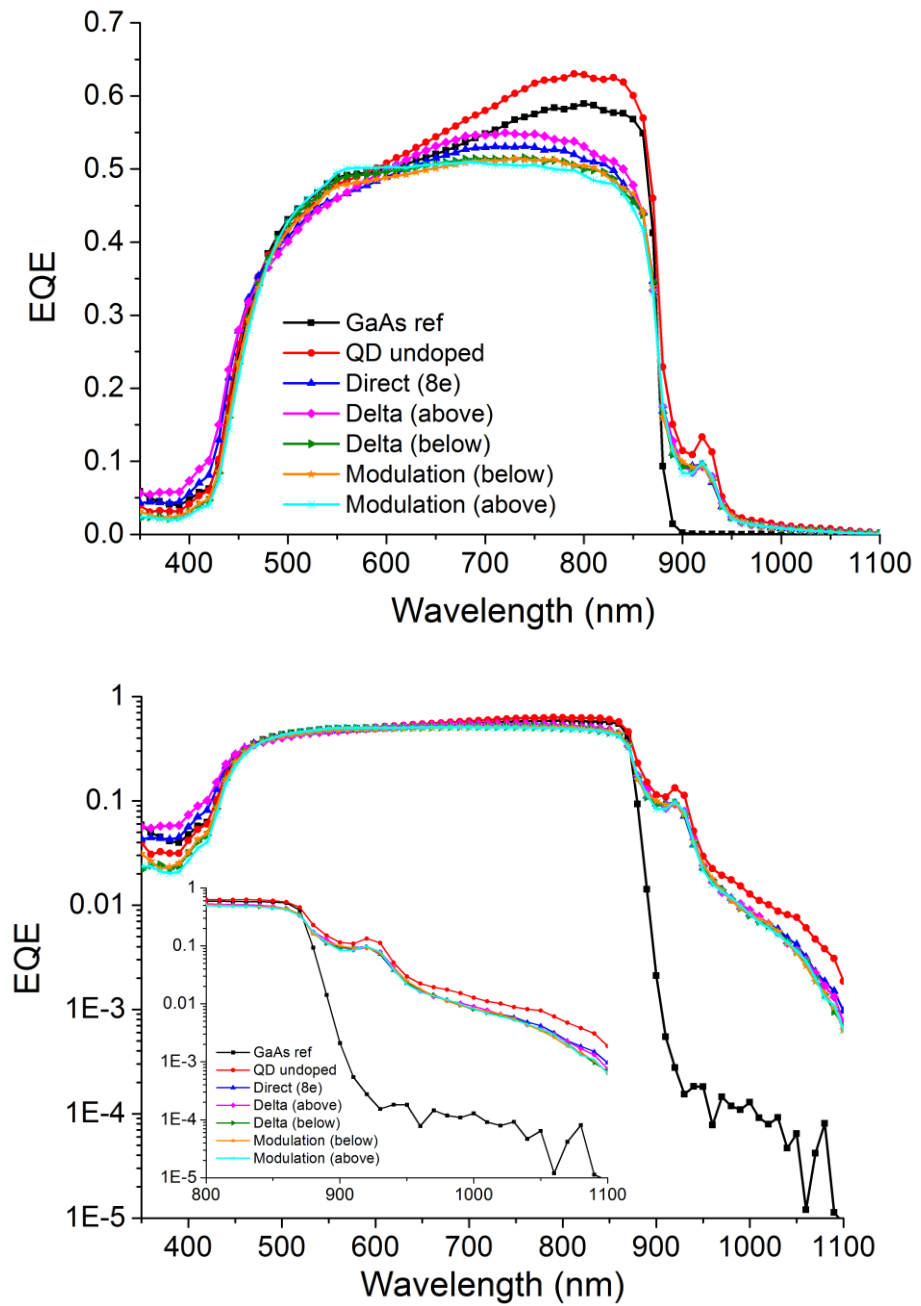
Figure 5.12 External quantum efficiency spectra for R3 - R9 in linear (top) and log (bottom) scale.

The J-V characteristics of the all samples are presented in Figure 5.13 and Table 5.1. All doped samples exhibit an improvement in V_{OC} compared to the undoped sample. This could be explained in terms of the reduced thermal coupling of QD states from the WL and CB in GaAs QDSCs assisted by Si doping. This reduced thermal coupling could be attributed to a potential barrier formed between the WL and QDs [4]. However, very little difference is observed between the different doping methods. All Si-doped samples display a significant drop in the current density when compared with the undoped sample. This can be related to the reduction in the EQE contribution from the supra-bandgap region observed in Figure 5.12. In other words, the decrease in the depletion region width caused by the introduction of Si dopants results in a reduction in the effective area for absorption, and hence a decrease in the current density.
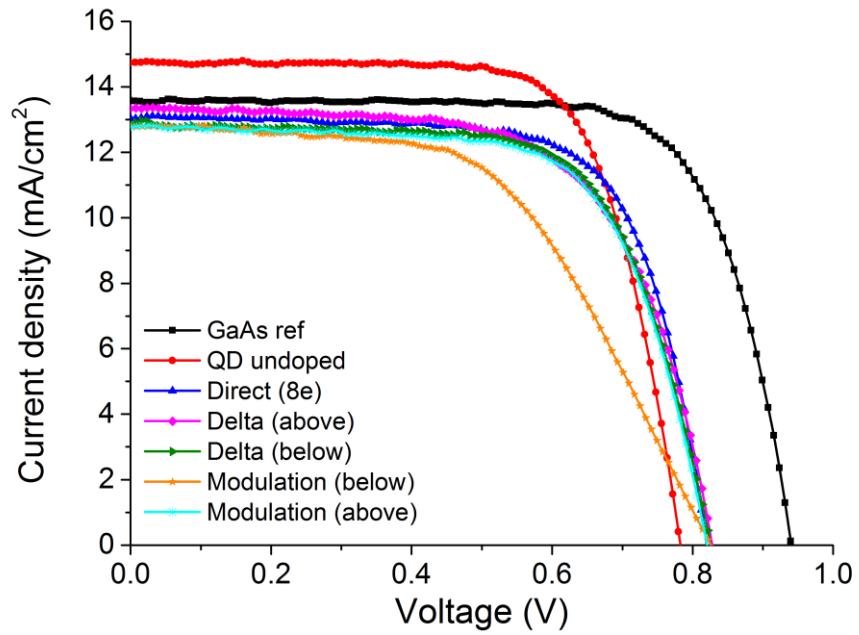
Figure 5.13 Current density vs. voltage measurements obtained under one sun (AM 1.5G) illumination for the best fill factor sub-samples.

Table 5.1 Short-circuit current (J_{SC}), open current voltage (V_{OC}), fill factor (FF), and efficiency (η) for R3 - R9 under 1 sun AM1.5 illumination at 25℃.

Device	J_{SC} (mA cm^{-2})	V_{OC} (mV)	FF (%)	η (%)
GaAs ref	13.57	940	73.4	9.4
QD undoped	14.75	782	71.7	8.3
Direct	13.08	820	70.4	7.5
Delta (above)	13.36	828	64.6	7.1
Delta (below)	12.90	826	68.0	7.2
Modulation (below)	12.81	826	55.0	5.8
Modulation (above)	12.8	820	67.9	7.1

5.3   Conclusion

In conclusion, QDSCs with different doping methods and positions, alongside two reference cells, have been grown by MBE and characterised by PL, EQE, and J-V measurements. PL results show a clear relationship between the degree of separation between the Si dopants and the QDs achieved by different doping methods, and the number of non-radiative recombination centres. All doped samples exhibited an increase in the V_{OC} by 40-46mV compared to the un-doped QDSC. Si-doping, however, lead to a drop in J_{SC} of ~ 13%, offsetting any potential improvement to the overall efficiency. Little difference could be observed between the different doping methods in terms of solar cell performances.

5.4   References

[1]   Y. Okada *et al.*, 'Increase in photocurrent by optical transitions via intermediate quantum states in direct-doped InAs/GaNAs strain-compensated quantum dot solar cell', *J. Appl. Phys.*, vol. 109, no. 2, p. 024301, Jan. 2011.

[2]   F. K. Tutu *et al.*, 'InAs/GaAs quantum dot solar cell with an AlAs cap layer', *Appl. Phys. Lett.*, vol. 102, no. 16, p. 163907, Apr. 2013.

[3]   I. Ramiro *et al.*, 'InAs/AlGaAs quantum dot intermediate band solar cells with enlarged sub-bandgaps', in *2012 38th IEEE Photovoltaic Specialists Conference (PVSC)*, 2012, pp. 000652–000656.

[4]   P. Lam *et al.*, 'Voltage recovery in charged InAs/GaAs quantum dot solar cells', *Nano Energy*, vol. 6, pp. 159–166, May 2014.

[5]   S. J. Polly, D. V. Forbes, K. Driscoll, S. Hellstrom, and S. M. Hubbard, 'Delta-Doping Effects on Quantum-Dot Solar Cells', *IEEE J. Photovolt.*, vol. 4, no. 4, pp. 1079–1085, Jul. 2014.

[6]   K. A. Sablon, J. W. Little, V. Mitin, A. Sergeev, N. Vagidov, and K. Reinhardt, 'Strong Enhancement of Solar Cell Efficiency Due to Quantum Dots with Built-In Charge', *Nano Lett.*, vol. 11, no. 6, pp. 2311–2317, 2011.

[7]   E. Antolin *et al.*, 'Advances in quantum dot intermediate band solar cells', in *2010 35th IEEE Photovoltaic Specialists Conference (PVSC)*, 2010, pp. 000065–000070.

[8] T. Morioka and Y. Okada, 'Dark current characteristics of InAs/GaNAs strain-compensated quantum dot solar cells', *Phys. E Low-Dimens. Syst. Nanostructures*, vol. 44, no. 2, pp. 390–393, Nov. 2011.

[9] H. F. Lu, L. Fu, G. Jolley, H. H. Tan, and C. Jagadish, 'Improved performance of InGaAs/GaAs quantum dot solar cells using Si-modulation doping', in *2012 Conference on Optoelectronic and Microelectronic Materials Devices (COMMAD)*, 2012, pp. 127–128.

[10] F. K. Tutu *et al.*, 'Improved performance of multilayer InAs/GaAs quantum-dot solar cells using a high-growth-temperature GaAs spacer layer', *J. Appl. Phys.*, vol. 111, no. 4, p. 046101, Feb. 2012.

[11] H. Y. Liu *et al.*, 'Improved performance of 1.3µm multilayer InAs quantum-dot lasers using a high-growth-temperature GaAs spacer layer', *Appl. Phys. Lett.*, vol. 85, no. 5, pp. 704–706, Aug. 2004.

[12] H. Y. Liu *et al.*, 'p-doped 1.3µmInAs/GaAs quantum-dot laser with a low threshold current density and high differential efficiency', *Appl. Phys. Lett.*, vol. 89, no. 7, p. 073113, Aug. 2006.

[13] H. Y. Liu *et al.*, 'Influences of the spacer layer growth temperature on multilayer InAs/GaAs quantum dot structures', *J. Appl. Phys.*, vol. 96, no. 4, pp. 1988–1992, Aug. 2004.

[14] X. Yang *et al.*, 'Improved efficiency of InAs/GaAs quantum dots solar cells by Si-doping', *Sol. Energy Mater. Sol. Cells*, vol. 113, pp. 144–147, Jun. 2013.

[15] X. Lu, J. Vaillancourt, and M. J. Meisner, 'A modulation-doped longwave infrared quantum dot photodetector with high photoresponsivity', *Semicond. Sci. Technol.*, vol. 22, no. 9, p. 993, 2007.

Chapter 6
Conclusions and future work

This chapter summarises the contributions of the work presented in this thesis towards understanding of the physics of solar cells, particularly in the quantum dot intermediate band solar cell based on III-V systems. However, as outlined in the previous chapters, there are outstanding issues that still need to be addressed to implement high-efficiency intermediate band solar cells. Therefore, alongside the conclusions from the work so far, this chapter includes suggestions for the direction of future research.

6.1 Conclusions

The concept of IBSC was proposed in an attempt to utilise sub-bandgap photons and overcome the Shockley-Queisser limit by introducing an IB within the bandgap [1]. In an ideal IBSC, sub-bandgap photon absorption via IB provides additional photocurrent generation without accompanying voltage reduction, which results in an increase in the power conversion efficiency. However, there have been many challenges in implementing

high-efficiency IBSCs. This research project aimed to provide solutions to some of the main challenges in realising QD-IBSCs based on using III-V semiconductor materials.

Firstly, the influence of direct Si doping on InAs/GaAs quantum dot solar cells with AlAs cap layers has been studied. State filling of the intermediate band, which is one of the key requirements for implementing a high-efficiency intermediate band solar cell has been achieved by Si-doping the QDs. Moreover, moderate levels of QD Si doping led to passivation of defect states, which prolonged the carrier lifetime, and hence, increased the V_{OC}.

Secondly, type-II InAs/GaAsSb quantum dot solar cells have been investigated. An increase in the sub-bandgap photocurrent has been achieved due to the prolonged carrier lifetime associated with the type-II band alignment.

Thirdly, different types of QD Si doping have been demonstrated. The photoluminescence spectra showed that using delta or modulation Si doping in QDs could reduce the degradation of crystal quality, reducing the number of non-radiative recombination centres compared with when direct QD Si doping was used.

6.2   Ongoing work

In previous studies, including [2] and the work presented in Chapter 3, we have observed that the supra-bandgap EQE and current density decrease once Si doping is introduced in quantum dots. This has been attributed to the decrease in the depletion region width, and hence the effective area of absorption of the solar cells. In order to recover the depletion width, Si-doped QDSCs with additional thickness of GaAs in the i-region are being studied. The additional GaAs layers are introduced in the spacer, emitter, and the base regions in three different QDSCs. Figure 6.1 shows the J-V characteristics from the preliminary measurements. It can be seen that introducing extra layer of emitter can lead to a higher current without too much loss in the high V_{OC} achieved by doping. This shows that the decrease in the depletion region width can be solved by optimising the i-region thickness.
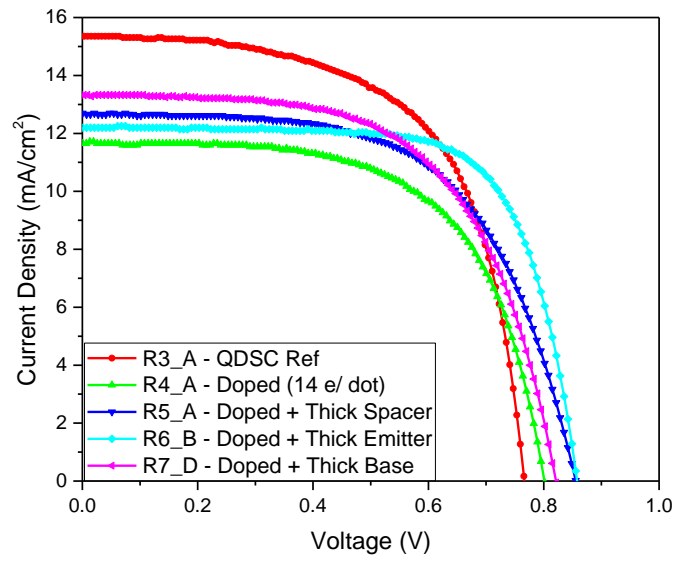
Figure 6.1 Current density vs. voltage characteristics for the reference solar cells and Si-doped QDSCs with additional i-GaAs layers.

Table 6.1 Current density, open-circuit voltage, fill factor, and efficiency measured from the reference solar cells and Si-doped QDSCs with additional i-GaAs layers

Device	I-region thickness (nm)	J_{SC} (mA/cm^2)	V_{OC} (mV)	FF (%)	η (%)
Undoped (R3_A)	420	15.38	775.88	61.85	7.38
Doped (R4_A)	420	11.66	800.74	62.06	5.80
Doped + Thick Spacer (R5_A)	520	12.64	854.96	60.58	6.55
Doped + Thick Emitter (R6_B)	520	12.19	857.63	71.14	7.44
Doped + Thick Base (R7_D)	520	13.33	820.49	60.24	6.59

6.3 Future work

In order to develop thin-film light-trapping enhanced QD-IBSCs with a high power conversion efficiency, it is essential to increase the photon absorption in QD arrays. To this end, plasmonic materials have previously been investigated [3]–[5]. Another alternative for increasing QD photon absorption is to increase the number of QDs by growing high-stack QD layers [6], or high in-plane density QD layers using Sb-mediated QD growth technique [7]. QDSCs with both high number of QD layers, and high in-plane QD density ($\sim 10^{11}$ cm^{-2}) have also not been demonstrated [8], [9], however, strain-induced dislocations in high-stack QD layers have resulted in deterioration of the solar cell performances. This leads to an opportunity to explore strain compensation technique using GaP layers [10] for the high-stack QD growth.

Although the development of QDSCs has been mainly driven by space and military applications, the importance of developing low cost QDSCs should not be overlooked. Having successfully demonstrated the first QD laser grown on Ge-on-Si substrate [11], and QD lasers directly grown on silicon substrates [12], UCL MBE Research Group has the capability for the growth of III-V QDSC on a Si substrate. The successful growth of III-V QDSC on Si will provide a significant advancement towards low-cost QDSC manufacturing.

6.4 References

[1] W. Shockley and H. J. Queisser, 'Detailed Balance Limit of Efficiency of p- n Junction Solar Cells', *J. Appl. Phys.*, vol. 32, no. 3, pp. 510–519, Mar. 1961.

[2] P. Lam *et al.*, 'Voltage recovery in charged InAs/GaAs quantum dot solar cells', *Nano Energy*, vol. 6, pp. 159–166, May 2014.

[3] H. F. Lu, S. Mokkapati, L. Fu, G. Jolley, H. H. Tan, and C. Jagadish, 'Plasmonic quantum dot solar cells for enhanced infrared response', *Appl. Phys. Lett.*, vol. 100, no. 10, p. 103505, Mar. 2012.

[4] J. Wu, S. C. Mangham, V. R. Reddy, M. O. Manasreh, and B. D. Weaver, 'Surface plasmon enhanced intermediate band based quantum dots solar cell', *Sol. Energy Mater. Sol. Cells*, vol. 102, pp. 44–49, Jul. 2012.

[5] J. Wu *et al.*, 'Strain-free ring-shaped nanostructures by droplet epitaxy for photovoltaic application', *Appl. Phys. Lett.*, vol. 101, no. 4, p. 043904, Jul. 2012.

[6] T. Sugaya *et al.*, 'Ultra-high stacks of InGaAs/GaAs quantum dots for high efficiency solar cells', *Energy Environ. Sci.*, vol. 5, no. 3, pp. 6233–6237, Mar. 2012.

[7] F. K. Tutu *et al.*, 'Antimony mediated growth of high-density InAs quantum dots for photovoltaic cells', *Appl. Phys. Lett.*, vol. 103, no. 4, p. 043901, Jul. 2013.

[8] F. Cappelluti *et al.*, 'Novel Concepts for High-Efficiency Lightweight Space Solar Cells', *E3S Web Conf.*, vol. 16, p. 03007, 2017.

[9] F. Cappelluti *et al.*, 'Light-trapping enhanced thin-film III-V quantum dot solar cells fabricated by epitaxial lift-off', *Sol. Energy Mater. Sol. Cells*, Jan. 2018.

[10] S. M. Hubbard, C. D. Cress, C. G. Bailey, R. P. Raffaelle, S. G. Bailey, and D. M. Wilt, 'Effect of strain compensation on quantum dot enhanced GaAs solar cells', *Appl. Phys. Lett.*, vol. 92, no. 12, p. 123512, Mar. 2008.

[11] H. Liu *et al.*, 'Long-wavelength InAs/GaAs quantum-dot laser diode monolithically grown on Ge substrate', *Nat. Photonics*, vol. 5, no. 7, pp. 416–419, Jul. 2011.

[12] S. Chen *et al.*, 'Electrically pumped continuous-wave III–V quantum dot lasers on silicon', *Nat. Photonics*, vol. 10, no. 5, pp. 307–311, May 2016.